


3-21-2017

# Orthoplanar Spring Based Compliant Force/ Torque Sensor for Robot Force Control

Jerry West

University of South Florida, [jerrywest@mail.usf.edu](mailto:jerrywest@mail.usf.edu)

Follow this and additional works at: <http://scholarcommons.usf.edu/etd>

 Part of the [Art Practice Commons](#), [Mechanical Engineering Commons](#), and the [Robotics Commons](#)

## Scholar Commons Citation

West, Jerry, "Orthoplanar Spring Based Compliant Force/Torque Sensor for Robot Force Control" (2017). *Graduate Theses and Dissertations*.

<http://scholarcommons.usf.edu/etd/6637>

This Thesis is brought to you for free and open access by the Graduate School at Scholar Commons. It has been accepted for inclusion in Graduate Theses and Dissertations by an authorized administrator of Scholar Commons. For more information, please contact [scholarcommons@usf.edu](mailto:scholarcommons@usf.edu).

Orthoplanar Spring Based Compliant Force/Torque Sensor  
for Robot Force Control

by

Jerry M. West

A thesis submitted in partial fulfilment  
of the requirements for the degree of  
Master of Science in Mechanical Engineering  
Department of Mechanical Engineering  
College of Engineering  
University of South Florida

Major Professor: Rajiv Dubey, Ph.D.  
Redwan Alqasemi, Ph.D.  
Craig Lusk, Ph.D.

Date of Approval:  
March 14, 2017

Keywords: Compliant Mechanisms, Robotic Wrist,  
Sensor Design, Calibration, Hall-effect Sensing

Copyright © 2017, Jerry M. West

### **Dedication**

I dedicate this thesis to my parents, Lynda and Mickey; my sisters, Darleen, Kimmy, and Monica; and my girlfriend, Kerri. Thank you all for the love and support.

### **Acknowledgements**

I would like to express gratitude to my major professor Dr. Rajiv Dubey for his guidance, encouragement, and support in my studies and research. Dr. Rajiv Dubey was quick to meet with me and share his immense wisdom and knowledge to help shape my research for the better.

I am very grateful to my committee members, Dr. Redwan Alqasemi and Dr. Craig Lusk. Dr. Redwan Alqasemi gave me the opportunity to work in his lab where he provided a great deal of useful advice and generously provided assistance in my research efforts. Dr. Craig Lusk shared many insights in research methods and ignited my interest in compliant mechanisms.

It has been great working with all the members of the Assistive Robotics Research lab at the University of South Florida. I would like to give a special thanks to Andoni Aguirrezabal, Karl Rothe, Lei Wu, and Shangdong Gong for your help in the lab.

## Table of Contents

List of Tables .....	iv
List of Figures .....	vi
Abstract .....	viii
Chapter 1: Introduction .....	1
1.1 Motivation .....	1
1.2 Thesis Objectives .....	1
1.3 Thesis Outline .....	2
Chapter 2: Background .....	3
2.1 Force Control .....	3
2.2 Passive Compliance, Force Control Dynamics, and Stability .....	4
2.3 Compliant Force/Torque Sensors .....	5
2.4 Compliant Mechanisms .....	7
2.5 Compliance Analysis .....	7
2.6 Hall-effect Sensing .....	7
Chapter 3: Sensor Design Considerations and Design Concept .....	8
3.1 Design Considerations .....	8
3.1.1 Measurement Axes .....	8
3.1.2 Measurement Range .....	9
3.1.3 Sensor Stiffness .....	9
3.1.4 Compactness .....	11
3.1.5 Sensor Accuracy .....	12
3.2 Design Concept .....	12
3.2.1 Orthoplanar Spring .....	13
3.2.2 Hall-effect Force Sensing .....	14
Chapter 4: Compliance and Stress Analysis, and Mechanical Design .....	15
4.1 Compliance Analysis .....	15
4.1.1 Effective Beam Length .....	15
4.1.2 Leg Compliance .....	17
4.1.3 Platform Compliance .....	20
4.2 Stress Analysis .....	21
4.3 Finite Element Analysis Validation of Compliance and Stress Analysis .....	22
4.4 Mechanical Design Method .....	23
4.4.1 Orthoplanar Spring and Mechanical Limit Iterative Design Procedure .....	23
4.4.2 Guidelines for Trial Parameter Selection .....	27
4.4.3 Base Structure and Mounting Component Design .....	28

Chapter 5: Three-Axis Hall-effect Transducer Modeling and Design.....	30
5.1 Kinematics and Statics.....	30
5.2 Magnetic Field Model.....	32
5.3 Hall-effect Sensor Response.....	33
5.4 Hall-effect Sensor and Magnet Selection and Placement.....	34
Chapter 6: Prototype Design and Construction.....	38
6.1 Prototype Design Specifications.....	38
6.2 Prototype Design.....	40
6.2.1 Orthoplanar Spring Design and Fabrication.....	41
6.2.2 Mechanical Limits: Design and Fabrication.....	43
6.2.3 Base Structure and Mounting Components: Design and Fabrication.....	43
6.2.4 Transducer Design.....	44
6.3 Prototype Assembly.....	45
6.4 Signal Processing.....	46
Chapter 7: Calibration and Testing.....	48
7.1 Sensor Calibration.....	48
7.1.1 Calibration Data Acquisition.....	48
7.1.2 Linear and Quadratic Calibration Laws.....	50
7.1.3 Calibration Laws Based on Physical Reasoning.....	52
7.1.4 Evaluation of Calibration Laws.....	56
7.2 Instrument Uncertainty.....	58
7.2.1 Sensor Drift.....	58
7.2.2 Instrument Repeatability.....	60
7.2.3 Sensor Noise.....	60
7.2.4 Overall Instrument Uncertainty.....	61
7.3 Discussion of Results.....	61
Chapter 8: Force Control Testing.....	63
8.1 Robot Kinematics and Motion Control.....	63
8.1.1 Robotic Arm Kinematics.....	63
8.1.2 Kinematics Control.....	65
8.2 Force Control Implementation.....	66
8.2.1 Hardware.....	66
8.2.2 Control Algorithm.....	66
8.3 Force Control Test Setup.....	67
8.3.1 Task Description.....	67
8.3.2 Force Control Law.....	68
8.3.3 Force Gain Selection.....	69
8.4 Comparison to Scale Tests.....	70
8.4.1 Results and Discussion.....	70
Chapter 9: Conclusions and Future Work.....	73
9.1 Summary of Work.....	73
9.2 Conclusions.....	73
9.3 Future Work.....	74

9.3.1 Design Variations .....	74
9.3.2 Stiffness Selection and Low Inertia End-Effector .....	74
References.....	76
Appendix A: Effective Beam Length Data .....	79
Appendix B: Stress Concentration Factor.....	80
Appendix C: Orthoplanar Spring Designs Used in Finite Element Analysis Validations .....	81
Appendix D: Copyright Permissions .....	82

## List of Tables

Table 4.1	FEA and theoretically determined stiffnesses.....	22
Table 4.2	FEA and theoretically determined maximum Von Mises stresses.....	23
Table 4.3	Orthoplanar spring parameters.....	24
Table 5.1	Transducer design parameters.....	36
Table 6.1	Sensor measurement ranges.....	38
Table 6.2	Sensor design stiffness, natural frequency, and maximum displacement.....	39
Table 6.3	Orthoplanar spring design parameters.....	42
Table 6.4	Footprint and compliance calculation results.....	42
Table 6.5	Comparison of FEA results and design calculations for the final prototype design.....	43
Table 6.6	Transducer design parameters.....	45
Table 7.1	Maximum and minimum values of applied forces and moments during calibration.....	50
Table 7.2	Curve fit parameters for physical reasoning based calibration law three.....	55
Table 7.3	Calibration root mean square errors and standard prediction errors.....	57
Table 7.4	Results of drift tests.....	59
Table 7.5	Standard deviations of repeatability test data.....	60
Table 7.6	Uncertainties due to instrument repeatability.....	60
Table 7.7	Standard deviation and uncertainty at 95% confidence of sensor noise.....	61
Table 7.8	Instrument uncertainty with and without drift error included.....	61
Table 8.1	D-H parameters of WMRA.....	64
Table 8.2	Force/torque sensor readings average and standard deviation.....	70
Table 8.3	Maximum and minimum force and moment indicated by the scale during steady-state.....	71
Table 8.4	Maximum error between sensor and scale measurements with increasing desired force.....	72



Table A.1	Data used to determine $f(b/c, b/h)$ .....	79
Table C.1	Design parameters of orthoplanar springs used in finite element analysis. ....	81

## List of Figures

Figure 2.1	Tasks requiring interaction between robot and environment.....	3
Figure 2.2	(a) Torque based force control (b) position based force control.....	4
Figure 3.1	Robot following unknown surface with 3-axis force/torque sensor. ....	8
Figure 3.2	Robot performing force controlled tasks with environment interaction forces and gravity. ....	9
Figure 3.3	Robot wrist with sensor illustrating footprint and height. ....	12
Figure 3.4	Orthoplanar spring with components labeled and sensor frame attached. ....	13
Figure 3.5	Single axis compliant force sensor using Hall-effect transducer.....	14
Figure 4.1	Geometry for determining effective beam length relationship using finite elements.....	17
Figure 4.2	Frame assignments and geometric parameters of orthoplanar spring.....	18
Figure 4.3	Setup and results of FEA with applied force. ....	22
Figure 4.4	Mechanical limit layout with numbering.....	24
Figure 4.5	Cantilevered beam with force at free end. ....	27
Figure 4.6	Iterative design procedure for orthoplanar spring and mechanical limits design. ....	29
Figure 5.1	General layout of magnets and Hall-effect sensors, (a) overhead view, (b) side view.....	31
Figure 5.2	Nominal Hall-effect sensor voltage output in response to magnetic field.....	33
Figure 6.1	Sensor-inertia model.....	40
Figure 6.2	Mechanical design of sensor.....	40
Figure 6.3	Rendering of compliant force/torque sensor integrated in robotic manipulator. ....	41
Figure 6.4	Transducer design of sensor. ....	41
Figure 6.5	Overall dimensions of sensor. ....	41
Figure 6.6	(a) Mechanical limit placement and design (b) mechanical limit itself.....	43

Figure 6.7	3D models of (a) the base structure and (b) upper and lower mount.....	44
Figure 6.8	(a) Hall-effect sensor and (b) magnet used in prototype. ....	45
Figure 6.9	Plot of the optimization criterion given by equation 5.27 vs. the placement parameter $s$ . ....	45
Figure 6.10	(a) Fabricated components and (b) completed prototype. ....	46
Figure 7.1	Attachment for applying forces and moments using weights.....	48
Figure 7.2	Three-dimensional plot of applied force and moment calibration data, $(M_x, M_z, F_y)$ .....	49
Figure 7.3	(a) Hall-effect sensor voltage vs. distance data and (b) linearized data. ....	55
Figure 7.4	Algorithm for determining initial force value at the start of the drift tests; (a) algorithm flow chart and (b) Matlab code implementing algorithm.....	59
Figure 8.1	Link parameters, joint variables, and link frames.....	64
Figure 8.2	Overview of hardware used to implement force control. ....	67
Figure 8.3	Force control algorithm flowchart.....	67
Figure 8.4	(a) test setup 1 using force measurement axis and (b) test setup 2 using moment axis of sensor.....	68
Figure 8.5	Force and moment plotted against time for varying gains. ....	69
Figure 8.6	Force and moment plotted against time for setup one and two respectively. ....	71
Figure 8.7	Sensor and scale data during testing with linearly increasing desired contact force.....	72
Figure A.1	Geometry for determining effective beam length relationship using finite elements. ....	79
Figure B.1	Stress concentration factor.....	80
Figure C.1	Design parameters of orthoplanar spring .....	81

## Abstract

A compliant force/torque sensor for robot force control has been developed. This thesis presents methods of designing, testing, and implementing the sensor on a robotic system. The sensor uses an orthoplanar spring equipped with Hall-effect sensors to measure one component of force and two moment components. Its unique design allows for simple and cost effective manufacturing, high reliability, and compactness. The device may be used in applications where a robot must control contact forces with its environment, such as in surface cleaning tasks, manipulating doors, and removing threaded fasteners. The compliant design of the sensor improves force control performance and reduces impact forces.

Sensor design considerations are discussed, followed by a discussion of the proposed design concept. Theoretical compliance and stress analysis of the orthoplanar spring is presented that allows for rapid design calculations; these calculations are validated via finite element analysis. A mechanical design method is given which uses the results of the compliance and stress analysis. Transducer design is then addressed by developing a model of the sensor. The design methods are used to design a prototype sensor which is tested to determine its instrument uncertainty. Finally, the sensor is implemented on a robotic platform to test its performance in force control.

## Chapter 1: Introduction

### 1.1 Motivation

The motivation for this work is the need for a cost-effective, compliant force/torque sensor for robot force control applications. Force/torque sensors are used in robotics applications where the robot is required to contact its environment. Force control may be accomplished by attaching a force/torque sensor to the wrist of the robot to provide force feedback, however, instability issues limit the performance of force control [16]. The situation is improved when there is compliance near the contact point, therefore, an effective method of improving the stability of force control is to design compliance into the force/torque sensor [11, 17].

Compliant mechanisms paired with contact free sensing should allow for the development of a cost-effective, compliant force/torque sensor. A primary motivation for this thesis is to investigate a design concept incorporating a compliant mechanism, known as an orthoplanar spring, and contact free sensing in the form of Hall-effect sensors. This design concept has advantages over previously designed multi-axis sensors. In conjunction with contact free sensing, the use of a compliant mechanism allows for low part count, simple assembly, and mechanical reliability [28]. Furthermore, contact free displacement sensing is well suited to compliant sensors because of the relatively large strains encountered [25].

### 1.2 Thesis Objectives

The main objective of this thesis is to develop a cost-effective compliant force/torque sensor for robotic force sensing applications. To that end, the objectives of this thesis are as follows:

1. Enumerate design considerations for a compliant force/torque sensor.
2. Propose a design concept based on an orthoplanar spring and Hall-effect sensing.
3. Analyze the mechanics of the proposed design concept to develop computationally efficient methods of accurately calculating compliance and stress.

4. Develop a mechanical design method for the proposed design concept.
5. Model the sensor for transducer design purposes as well as calibration laws based on physical reasoning.
6. Construct a prototype of the proposed force/torque sensor.
7. Compare various calibration laws for the sensor.
8. Perform tests to characterize the sensor and determine its instrument uncertainty.
9. Implement the sensor on a robotic system in force control to validate the sensor's design.

### **1.3 Thesis Outline**

The remainder of this thesis is divided into eight chapters. Chapter 2 covers background works in robot force control; the interplay between robot dynamics, stability, and compliance; previously designed compliant force sensors; compliant mechanisms; compliance analysis; and Hall-effect sensing. In Chapter 3, sensor design considerations are enumerated and discussed followed by a description of the proposed design concept. Chapter 4 presents methods of compliance and stress analysis and the sensor mechanical design method that was developed. Chapter 5 presents models of the sensor and applies them to the transducer design of the sensor. In chapter 6, the prototype design and its construction are discussed, followed by its calibration, testing, and uncertainty evaluation in Chapter 7. Chapter 8 discusses the implementation of the sensor on a robotic system, and the force control tests that were performed. Finally, Chapter 9 discusses conclusions and future work.

## Chapter 2: Background

### 2.1 Force Control

There are many tasks requiring a robot to interact with its environment [1]. In such tasks, the end-effector's trajectory must be modified in response to contact forces to comply with the constraints of the task configuration [2], examples of such tasks are illustrated in Figure 2.1. Force control relies on force measurements from the robot's sensors to modify the end-effectors trajectory using feedback control. Many different force control algorithms have been proposed by researchers over the last 40 years, however, the two major approaches to force control are hybrid position/force control and impedance control [3].

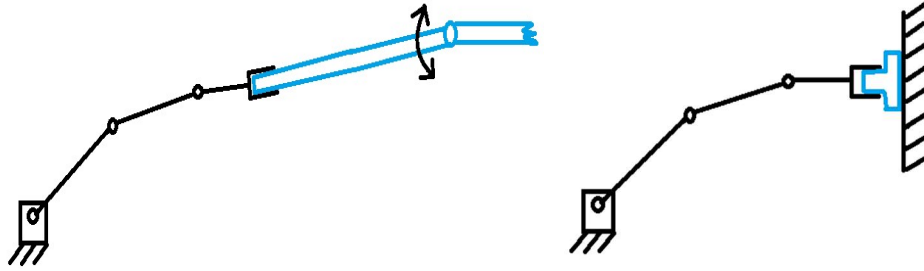


**Figure 2.1:** Tasks requiring interaction between robot and environment.

One of the first force control algorithms was Whitney's damping control, where end-effector velocity commands are modified by a linear force feedback strategy [4]. Salisbury developed a method of actively controlling the stiffness of the end-effector by transforming the desired Cartesian stiffness into joint-space [5]. Impedance control expanded on Whitney's damping control and Salisbury's active stiffness control, resulting in a general approach to manipulation where the end-effector is made to behave as an impedance with a desired stiffness, damping, and inertia [6].

The other major approach to force control is hybrid position/force control. A formal model of position and force control was developed in [2], which provided a framework for the hybrid position/force control architecture developed by Raibert and Craig [7]. Hybrid position/force control assumes the end-

effector is controlled in a constraining environment; position constraints and force constraints arise from the mechanical and geometric characteristics of the task configuration. The hybrid position/force control approach divides the task degrees-of-freedom into force and position controlled subsets; forces are controlled in position constrained degrees-of-freedom and position is controlled in force constrained degrees-of-freedom. The hybrid position/force controller is simultaneously able to control force and position along different degrees-of-freedom.

Impedance and hybrid position/force control approaches can be implemented using either a torque based or an inner position loop based scheme [6, 8]. In torque based schemes, joint torque commands are computed directly from control errors. In inner position loop based schemes, motion commands are computed from force control errors- then an inner position loop computes the command torques [9], see Figure 2.2. Force control based on an inner position loop has several advantages over torque based control, most notably inner position loop based controllers have greater disturbance rejection capabilities [9]. Furthermore, most robots in common use today have a position control interface rather than a torque control interface; position loop based control is therefore well suited to these robots [10].

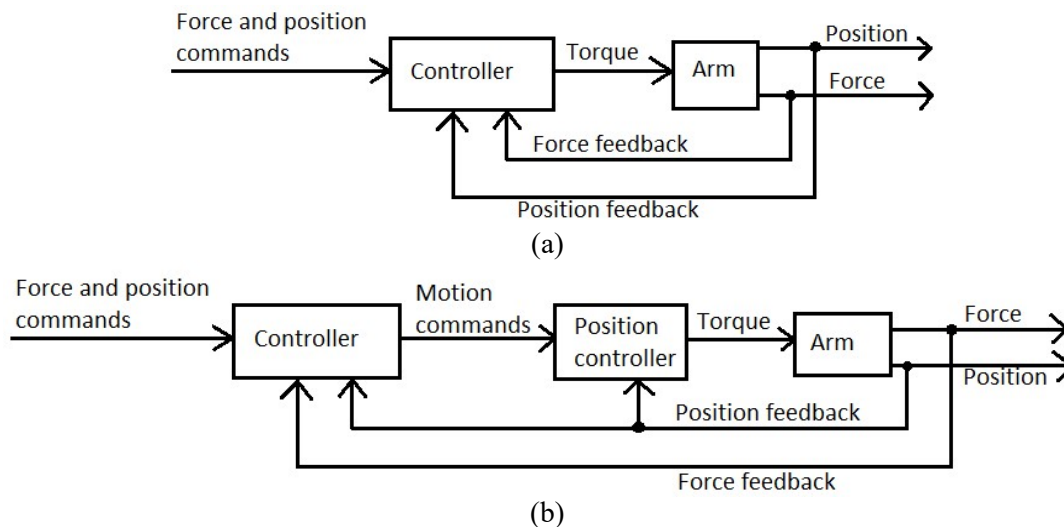


**Figure 2.2:** (a) Torque based force control (b) position based force control.

## 2.2 Passive Compliance, Force Control Dynamics, and Stability

It has been well established both theoretically and experimentally that passive compliance near the contact point has a beneficial effect on the stability of force control [4, 11, 12, 13]. A system that is more



stable can also be made more responsive; this is because control gains may be increased without causing instability. Dynamic models of damping force control developed by Whitney showed that the allowable force control gains were proportional to the contact compliance [4]. Whitney found that if the control gains are too large, unstable behavior results because of the time delays associated with digital sampling. A systematic experimental study on the effect of wrist force sensor stiffness on force control was carried out in [11], it was found that a sensor with lower stiffness permitted more responsive force control. Whitney pointed out in his paper that time delays due to digital sampling rates are not the only cause of bandwidth limitations in force control. Indeed, through further study of dynamic models of force control, Eppinger and Seering found that important drivers of instability are the joint and structural flexibilities of the robot as well as limitation in actuator bandwidth [12]. In contrast, it was found that sensor and workpiece compliances typically do not cause instability. Force controlled two-link flexible joint and flexible-link manipulators with a compliant force sensor were modeled in [13], it was found that a lower stiffness sensor results in a more stable system, in agreement with Eppinger and Seering's models. Finally, relationships between compliance and several force control performance parameters were derived in [8], leading to the conclusion that passive compliance can increase task execution speed and improve disturbance rejection of the force controller.

Contact tasks have three stages: free-space motion, transition, and constrained motion [14]. An impact will typically occur during the transition phase [15]. In [14], it was found experimentally that some level of compliance is necessary to achieve stable impact control and it was pointed out that it is unreasonable for a manipulator to react to impact forces if the contact is too stiff. In [11] and [8] it was found that the use of a more compliant sensor allowed for greater approach velocities before instability occurred.

### **2.3 Compliant Force/Torque Sensors**

The research on the effects of contact compliance in force control led to the development of compliant force/torque sensors; this approach to force control has been termed hybrid active/passive control [16]. In [17], an instrumented compliant wrist was developed with a compliant structure made up of rubber

elements. The deflection of this compliant structure was sensed by a six-link serial mechanism equipped with potentiometers at its joints, allowing the wrist to sense displacements in all six-axes. With a known stiffness matrix of the compliant structure, six-axes of force and moment can be deduced from the sensor's output. A compliant wrist with a similar type of design was developed in [18] where the accuracy of the wrist was discussed. It was found that hysteresis is the most significant error source and that hysteresis of the rubber elements and friction in the joint potentiometers were factors contributing to the hysteresis error. A three-axis compliant force sensor was developed in [19], which is based on a parallel mechanism. The compliant structure of this sensor is produced by incorporating linear spring-dampers into a three degree-of-freedom parallel mechanism; linear potentiometers are used to sense the mechanisms deflections in the three-axes.

More recently, compliant force sensors have been developed which use contact free sensing rather than a mechanism equipped with potentiometers. In [20], a compliant structure was designed which uses flexible beam segments. A sensing approach based on fiber optic displacement sensing was proposed to sense the compliant displacement of this compliant structure, but this approach has not yet been implemented. The sensed displacement of this sensor would be used to deduce forces and moments by multiplying by the compliant structure's stiffness matrix. Fiber optic sensing has been used in the construction of a single-axis force sensor using an orthoplanar spring elastic element [21]. Besides fiber optic sensing, other contact free sensing methods include capacitive sensing, such as in [22], and Hall-effect sensing which was employed in [23]. Strain gages, which are typically used in stiff force sensors, have a very high sensitivity and tend not to be used in compliant sensors [24]. Strain gages also have other disadvantages such as having complicated mounting procedures and complex signal conditioning [25].

Compliant force sensors have been applied in a variety of applications. A compliant force/torque sensor was used on a domestic service robot for improved stability in surface cleaning tasks [26]. The compliant sensor in [20] is intended for use in automated medical ultrasound probes to ensure safety of the patient. In [27], it was pointed out that different requirements apply to force sensors for human-robot interaction, namely, the sensor may be more compliant and have fewer degrees-of-freedom. Compliant

force sensors are most applicable when compliant motion is a higher priority than high speed positioning and load carrying capability.

## **2.4 Compliant Mechanisms**

A critical element in the design of a compliant force sensor is the method of achieving compliant behavior. One possibility is a compliant mechanism. A compliant mechanism is a mechanism that gains mobility through the deflection of its flexible members [28]. Compared to the compliant wrist designs in [17], [18], and [19], which employ traditional rigid-body mechanisms together with compliant elements, a device using only a compliant mechanism has several advantages, including lower part-count, simplified assembly, low cost manufacture, reduced wear, and fewer or no joints [28]. There are, however, disadvantages of compliant mechanisms including greater possibility of creep and stress relaxation [28].

## **2.5 Compliance Analysis**

Compliant mechanisms may undergo large deflections requiring non-linear analysis methods using elliptic integrals or the pseudo-rigid-body model, however, if the mechanism is limited to small deflections, then a linear analysis is adequate [28]. Compliance analysis is a linear analysis method used to determine the force-deflection relationship of a general flexure, or a compliant mechanism [29]. In compliance analysis, the compliance of the individual elements making up the compliant mechanism are determined; these individual compliances are then combined analytically to determine the compliance of the mechanism [29]. Compliance analysis has been used to determine the stiffness of a vibratory bowl feeder device [30] and orthoplanar springs [31].

## **2.6 Hall-Effect Sensing**

The Hall effect refers to the development of a voltage transversely across a current-carrying conductor in the presence of a magnetic field perpendicular to the current [32]. A magnetic-field sensor based off this effect is termed a Hall-effect sensor. Hall-effect sensors can be used to sense position when paired with a magnet, as in [33], and if a magnet is attached to an elastic element, force can be sensed [34].

## Chapter 3: Sensor Design Considerations and Design Concept

In this chapter, design considerations for force/torque sensors are introduced, including measurement axes, measurement range, stiffness, compactness, and accuracy. These design considerations form the basis of design methods presented in chapters 4 and 5, which were used to design the sensor presented in this thesis. Next the design concept of the developed sensor is discussed followed by an overview of its two main components: an orthoplanar spring and Hall-effect force sensing.

### 3.1 Design Considerations

#### 3.1.1 Measurement Axes

The tasks a robot is to perform will determine the components of force and torque the sensor must measure. Measured components of force and torque must correspond to directions in which force control is used. An example of a force control task is a robot following an unknown surface, as shown in Figure 3.1. In this case, a three measurement-axis sensor is required for the end-effector to actively comply to the surface [19]. Feedback in these measurement axes allows the robot to sense and correct misalignments about the X and Z axes and maintain a constant contact force along the Y-axis. A six-axis force/torque sensor allows force control in any direction and is therefore more adaptable, however, in many applications a three-axis sensor is sufficient or desirable. A compliant sensor may be made stiff in degrees-of-freedom where force is not measured, thus a three-axis sensor may be especially desirable for the case of a compliant sensor because of the reduced vibrational and deflection modes possible. Finally, at least one transducer is required for each measurement axis, therefore a smaller number of measurement axes reduces complexity of the sensor.

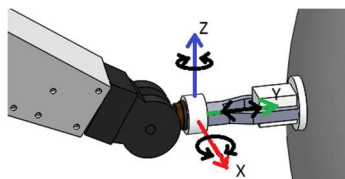


**Figure 3.1:** Robot following unknown surface with a 3-axis force/torque sensor.

### 3.1.2 Measurement Range

The measurement range of a force/torque sensor may be specified by a minimum and maximum force or moment that can be measured in each axis. The measurement range of a force sensor may be limited by stresses or nonlinearities within the elastic element of the sensor, or by limitations of the transducers used to measure elastic element's deformation. A force/torque sensor should be able to measure forces and moments large enough to accommodate the forces and moments required for force controlled tasks, as well as loadings due to end-effector and payload weight and friction forces. A robot performing a force controlled task is shown in Figure 3.2. The sensor should be designed to measure forces,  $F_s$ , and moments,  $M_s$ , for the expected gravitational and environmental forces, which are related by

$$F_s = W + F_{env} \quad (3.1)$$

and

$$M_s = r_{cg} \times W + r_{env} \times F_{env} \quad (3.2)$$

Often the robot will need to perform many different types of tasks, especially in rehabilitation and assistive applications; in these cases, the tasks with the largest applied forces and moments should be analyzed to determine an adequate measurement range.

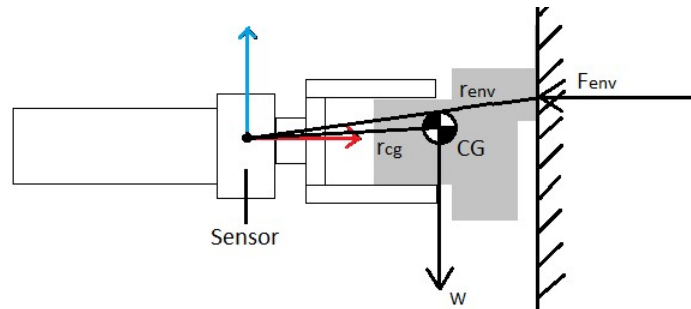


**Figure 3.2:** Robot performing force controlled tasks with environment interaction forces and gravity.

### 3.1.3 Sensor Stiffness

Stiffness affects performance during position and force control. In position control, low stiffness means larger static deflections as well as larger oscillations. The static deflections of the sensor lead to position errors given by

$$\delta X = TK_s^{-1}T^T F \quad (3.3)$$

where

$\delta X =$  End-effector displacement vector (position and orientation) due to sensor deflection

$T =$  Transformation matrix relating sensor deflections to end-effector displacement

$K_s =$  Sensor stiffness matrix

$F =$  Force and moment vector acting on end-effector

The compliance of the sensor also reduces the natural frequency of the robot. The sensor acts as a generalized spring with end-effector and payload inertia attached. Assuming the sensor is fixed on a rigid base and only small deflections occur with minimal damping, the equations of motion of the sensor-inertia system are given by

$$M\ddot{Y} + K_s Y = F_s \quad (3.4)$$

where

$M =$  Mass matrix of inertia attached to sensor

$Y =$  Displacement of sensor

$F_s =$  Force and moment vector acting on the sensor

The eigenfrequencies of this system are the square root of the eigenvalues given by

$$\Lambda = \text{Eigenvalues}(M^{-1}K) \quad (3.5)$$

The lowest eigenfrequency is the most important to know in practice [35], this is because the robot must operate below this frequency in order to avoid resonance.

In force control, low stiffness results in greater responsiveness [11]. The use of a compliant sensor ensures that the effective contact stiffness is low, resulting in several benefits during force control tasks, including increased task execution speed; improved force resolution; and in the case of inner position loop based force control, reduced force disturbance effects on the inner position control loop [8]. In [8], a parameter was defined which is important in determining the tracking and impact control performance of a

force controlled robot. The parameter was defined for one-dimensional integral force control based on an inner position loop, such a control law can be written as

$$X_d = k_c^{-1} k_{fi} \int (F_d - F) dt \quad (3.6)$$

or

$$\dot{X}_d = k_c^{-1} k_{fi} (F_d - F) \quad (3.7)$$

This control law can be recognized as a form of damping control introduced by Whitney in [4]. The parameter mentioned above is given by

$$K_{vx} = k_c^{-1} k_{fi} \quad (3.8)$$

where  $k_c$  is the contact compliance and  $k_{fi}$  is the integral force gain. This parameter comes from the analysis of steady state force error that arises because of relative motion between the robot and workpiece; this force error is given by [8]

$$\Delta F_{ss} = K_{vx}^{-1} V_{env} \quad (3.9)$$

Therefore, the steady-state force error is proportional to the contact stiffness. In the worst-case scenario, the robot will encounter a stiff environment, in this case the contact stiffness is approximately the stiffness of the force sensor. The steady-state force error can also be reduced by increasing  $k_{fi}$ , however,  $k_{fi}$  is limited by the positioning bandwidth of the robot [8].

In some robotics applications, high stiffness is necessary for the robot to cope with large loads and high speed motions; in these cases, a compliant sensor is not appropriate. There are other robotics applications where positioning accuracy are less critical, while the ability of the robot to compliantly interact with its environment safely and reliably is crucial. In these applications, it may be desirable to use a compliant sensor.

### 3.1.4 Compactness

An ideal sensor would take up no space, therefore a force/torque sensor should be as compact as possible. Sensor compactness can be divided into two components, footprint and height as illustrated in Figure 3.3. Sensor footprint is a measure of how much the sensor protrudes out of the robot, and height is

the length the sensor adds to the wrist of the robot. Footprint diminishes the robot's ability to fit through narrow openings, while height may have undesirable effects on the robot's kinematics.

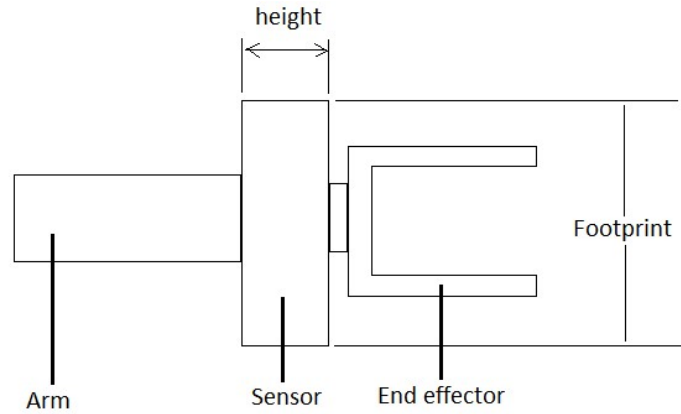


**Figure 3.3:** Robot wrist with sensor illustrating footprint and height.

### 3.1.5 Sensor Accuracy

Sensor error limits the ability of the robot to precisely sense and interact with its environment. Sensor measurement accuracy refers to how closely the measurements provided by the sensor agree with the true value being measured, however, because the true value will be unknown, the probable range of error is estimated by the measurement uncertainty [36]. The measurement errors of a force/torque sensor were attributed to calibration prediction errors, noise, and drift in [37]. In general, instrument uncertainty may be attributed to other errors as well, such as hysteresis and repeatability [36]. The overall uncertainty of a force/torque sensor is influenced by transducer placement, signal conditioning, assembly, and the mechanical design.

### 3.2 Design Concept

The compliant force/torque sensor developed in this thesis is based on an orthoplanar spring elastic element using Hall-effect sensing to sense its deflections. The orthoplanar spring provides beneficial passive compliance in three axes, therefore, an orthoplanar spring is suitable for compliant 3-axis force/torque sensing. Force and torque measurements are obtained by processing Hall-effect sensor outputs, which respond to the displacement of magnets mounted in the center platform of the orthoplanar spring.



Orthoplanar springs are compact and simple to manufacture due to their planar nature; Hall-effect sensors are low cost, reliable, contact free, and relatively easy to implement. Furthermore, no links or joints are required, thus there is minimal wear. The above advantages are thought to make the present design part of a cost effective and reliable solution to responsive and stable force control.

### 3.2.1 Orthoplanar Spring

A force/torque sensor measures forces and moments using the deformations or displacements of its elastic element; the concept developed in this thesis uses an orthoplanar spring as its elastic element. An orthoplanar spring is a compliant mechanism that is fabricated in a plane while allowing displacements out of its plane of fabrication [38]. The main components of an orthoplanar spring include a base, several legs, and a platform; the legs are themselves made up of flexible beams which are connected by connectors [38]. Many variations are possible and can be categorized by number of legs, number of beams per leg, and the angle that the legs are attached to the platform [38]. The orthoplanar spring chosen for the prototype has three legs that are angled parallel to the sides of the platform, further, each leg has two flexible segments. This type of orthoplanar spring is shown in Figure 3.4. This orthoplanar spring has the minimal number of flexible segments required to avoid stress stiffening. Furthermore, three legs provide greater rotational stability compared to four leg designs [38]. Five or more legs may be used, however the compactness of the sensor would be negatively affected.

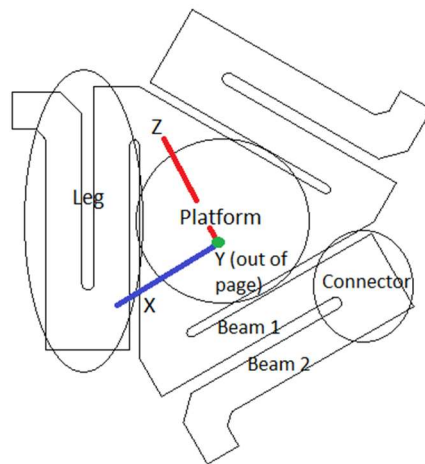


**Figure 3.4:** Orthoplanar spring with components labeled and sensor frame attached.

Orthoplanar springs are capable of large displacements without undergoing rotation about the axis out of the plane of fabrication [38]. Referring to Figure 3.4, orthoplanar springs are compliant in rotation about the X and Z-axes and translation along the Y-axis and relatively stiff in the other degrees-of-freedom [31]. Moments may therefore be sensed about the X and Z-axes and force may be sensed along the Y-axis.

### 3.2.2 Hall-effect Force Sensing

Hall-effect sensors can be used to sense the position of a magnet. Therefore, by mounting magnets on an elastic element, Hall-effect sensing can be used to sense the deflection of an elastic element allowing the force acting on it to be deduced. A simple force sensor using a Hall-effect transducer is shown in Figure 3.5. A force acting on the elastic element causes a displacement of the attached magnet. The displacement of the magnet results in a change in magnetic field at the Hall-effect sensor. The Hall-effect sensor outputs a voltage signal in proportion to this change in magnetic field via the Hall-effect principle. The force acting on the elastic element can thus be deduced from the voltage output of the Hall-effect sensor. This example demonstrates the Hall-effect force sensing concept in one axis, which is extended to achieve three-axis sensing in the developed force/torque sensor.

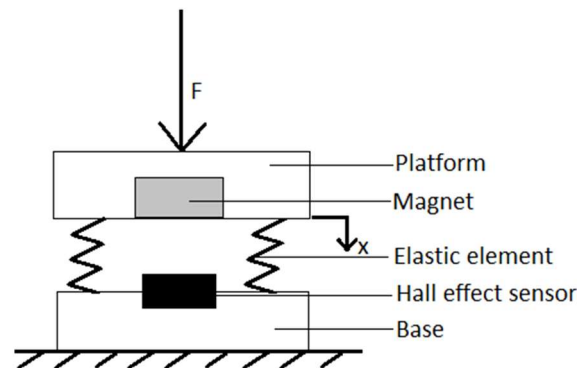


**Figure 3.5:** Single-axis compliant force sensor using Hall-effect transducer.

## Chapter 4: Compliance and Stress Analysis, and Mechanical Design

To facilitate rapid design iterations during the early design stage of the sensor, computationally efficient analytical expressions for the compliance properties and maximum stresses of the orthoplanar spring were developed. In [31], expressions for each element of the compliance matrix of an orthoplanar spring were derived. In this study, the results of the compliance analysis in [31] are used, however, one of the assumptions was dropped to obtain better agreement with FEA results, namely, the connector element between the beam segments of the orthoplanar spring was no longer assumed to be rigid. In this chapter, the compliance matrix of the central platform is expressed in terms of the geometric and material properties of the orthoplanar spring. A method of calculating stresses is then introduced. Finally, a mechanical design method is discussed covering the design of the orthoplanar spring and mechanical limits, as well as the sensor's base and mounting components.

### 4.1 Compliance Analysis

Compliance analysis was used to determine the compliance of the central platform and each of the legs of the orthoplanar spring. A general formulation of linear compliance analysis is presented in [29]. This general formulation was applied to the case of an orthoplanar spring in [31], where closed form expressions for each element of the compliance matrix were found. The equations derived in [31] assume the connector is rigid, however, finite element analysis of a preliminary design revealed that the connector possessed significant compliance. To account for connector compliance, the results derived in [31] were modified by increasing the effective length of the orthoplanar spring's beams in the compliance analysis.

#### 4.1.1 Effective Beam Length

The compliance of the connector, shown in Figure 3.4, is accounted for by increasing the effective length of the orthoplanar spring's beams. To find the increase in effective beam length, finite element simulations were performed on an isolated beam segment-connector geometry, as shown in Figure 4.1. The

boundary conditions applied were similar to that experienced by the beam segment-connector geometry as part of the orthoplanar spring. The results of the finite element analysis indicated that the increase in effective beam length required is approximately independent of the connector width and beam length if they are adequately large. In this case, the effective beam length increase depends only on beam width, connector length, and beam thickness. Dimensional analysis was used to reduce the number of variables involved in the finite element tests, resulting in

$$\frac{\delta L_{eff}}{c} = f\left(\frac{b}{c}, \frac{b}{h}\right) \quad (4.1)$$

where  $\delta L_{eff}$  is the change in effective beam length due to the connector,  $c$  is half the connector length,  $b$  is the beam width, and  $h$  is the orthoplanar spring thickness.

In conjunction with Euler-Bernoulli beam theory, data collected from finite element analysis simulations was used to determine the function  $f\left(\frac{b}{c}, \frac{b}{h}\right)$ . Euler-Bernoulli beam theory was used to determine the theoretical force-deflection relationship of the end of a beam with a transverse force applied at its end. This deflection is given by

$$\delta = \frac{FL^3}{3EI} \quad (4.2)$$

where  $F$  is the transverse force,  $L$  is the beam length,  $E$  is the elastic modulus, and  $I$  is the beam's second moment of area. Finite element simulations were performed on the geometry in Figure 4.1 to find the deflection of the beam end, which includes the effects of connector compliance. The deflections found in the finite element simulations were used to compute an effective beam length found by solving equation 4.2 for length; this calculated length is given by

$$L_{eff} = \left(\frac{3EI\delta}{F}\right)^{\frac{1}{3}} \quad (4.3)$$

The change in effective length is then given by

$$\delta L_{eff} = L_{eff} - L \quad (4.4)$$

This change in beam length was found for  $b/c$  and  $b/h$  values covering the considered design space.

The function  $f\left(\frac{b}{c}, \frac{b}{h}\right)$  was found using a first order polynomial least squares fit given by

$$\frac{\delta L_{eff}}{c} = 0.3694 \left(\frac{b}{c}\right) - 0.0569 \left(\frac{b}{h}\right) + 0.9239 \quad (4.5)$$

The root-mean-square error for this curve fit was calculated by

$$RMS_{error} = \sqrt{\frac{1}{m-3} \sum_{i=1}^m \left[ \left( \frac{\delta L_{eff}}{c} \right)_{curve} - \left( \frac{\delta L_{eff}}{c} \right)_{data} \right]^2} \quad (4.6)$$

For the data gathered  $RMS_{error} = 0.1098$  with an R-squared value of 0.9938. Furthermore, the maximum relative error of the fit is 9.8 %. The data is given in Appendix A.

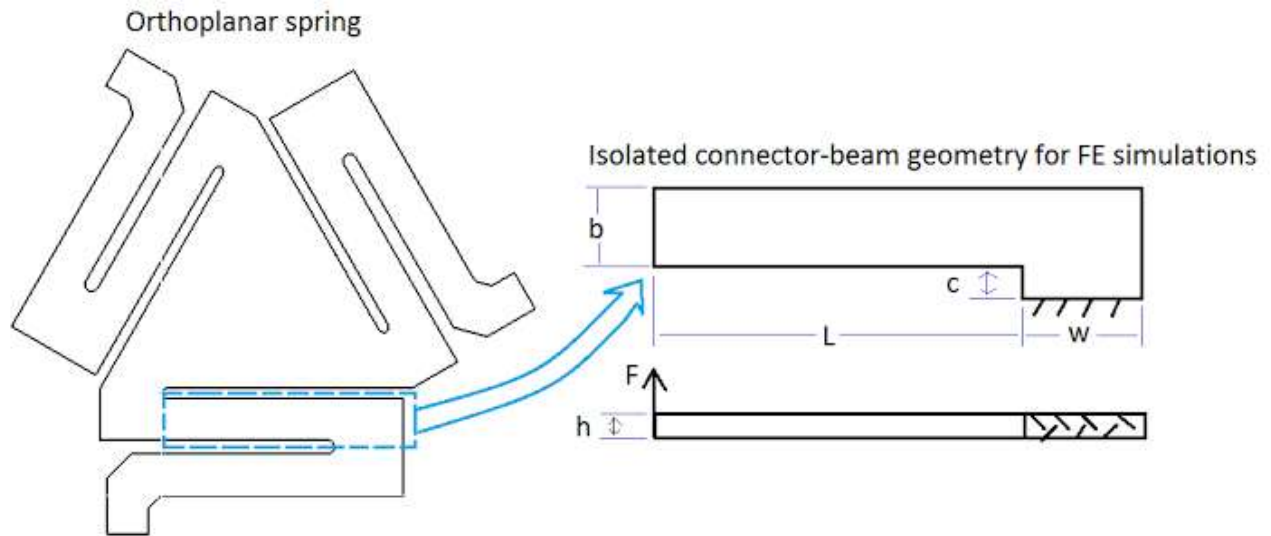


**Figure 4.1:** Geometry for determining effective beam length relationship using finite elements.

#### 4.1.2 Leg Compliance

The compliance of the  $j$ th leg can be determined by transforming the compliance matrix of each beam into a common leg frame  $\{O_j\}$ ; adding the compliance of each beam in this frame then yields the compliance matrix of the leg [31]. Following the analysis in [31], the coordinate frames used in the following analysis are shown in Figure 4.2. Each leg has a similar set of frames.

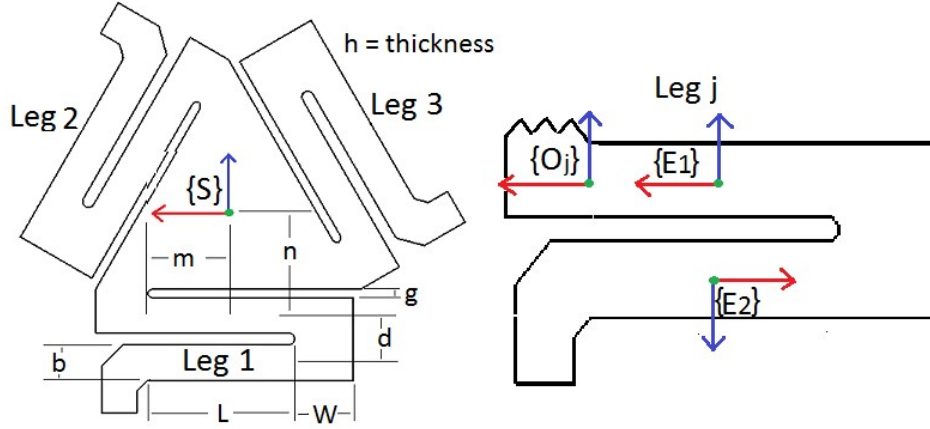


**Figure 4.2:** Frame assignments and geometric parameters of orthoplanar spring.

In the literature on compliance analysis, such as [31], it is well known that the compliance matrix of a beam segment, written in the beam's elastic center frame  $E_i$ , is given by

$$C_b = \text{diag} \left[ \frac{L_{eff}}{EA} \quad \frac{L_{eff}^3}{12EI_z} \quad \frac{L_{eff}^3}{12EI_y} \quad \frac{L_{eff}}{GI_x} \quad \frac{L_{eff}}{EI_y} \quad \frac{L_{eff}}{EI_z} \right] \quad (4.7)$$

where in this work  $L_{eff}$  is used instead of  $L$ .  $I_x$  is the beam's torsional constant given by

$$I_x = bh^3 \left( \frac{1}{3} - 0.21 \left( \frac{h}{b} \right) \left( 1 - \frac{h^4}{12b^4} \right) \right), \text{ when } \frac{h}{b} \leq 1 \quad (4.8)$$

and  $I_y$  and  $I_z$  are the area moment of inertias about y and z respectively, given by

$$I_y = \frac{1}{12} hb^3 \quad (4.9)$$

and

$$I_z = \frac{1}{12} bh^3 \quad (4.10)$$

Now, the leg compliance matrix may be written as

$$C_{leg} = {}^{O_j}T C_b {}^{O_j}T^T + {}^{O_j}T C_b {}^{E_2}T^T \quad (4.11)$$

where  ${}^{O_j}T$  and  ${}^{E_2}T$  are transformation matrices that transform displacements in  $E_1$  and  $E_2$  respectively into displacements in frame  $O_j$ . Each of the transformation matrices are given by

$${}_{Ei}^{Oj}T = \begin{bmatrix} {}_{Ei}^{Oj}R & -{}_{Ei}^{Oj}R {}_{Oj}^{Ei}P \\ 0 & {}_{Ei}^{Oj}R \end{bmatrix} \quad (4.12)$$

where  ${}_{Ei}^{Oj}R$  are rotation matrices of frame  $Ei$  relative to frame  $Oj$ .  ${}_{Oj}^{Ei}P$  are skew symmetric cross product matrices of the position of the origin of frame  $Oj$  in frames  $Ei$ . The rotation matrices are evaluated as

$${}_{E1}^{Oj}R = \begin{bmatrix} 1 & 0 & 0 \\ 0 & 1 & 0 \\ 0 & 0 & 1 \end{bmatrix} \quad (4.13)$$

and

$${}_{E2}^{Oj}R = \begin{bmatrix} -1 & 0 & 0 \\ 0 & 1 & 0 \\ 0 & 0 & -1 \end{bmatrix} \quad (4.14)$$

and the skew symmetric cross product matrices are evaluated by

$${}_{Oj}^{E1}P = \begin{bmatrix} 0 & 0 & 0 \\ 0 & 0 & -\frac{L_{eff}}{2} \\ 0 & \frac{L_{eff}}{2} & 0 \end{bmatrix} \quad (4.15)$$

and

$${}_{Oj}^{E2}P = \begin{bmatrix} 0 & -\frac{d}{2} & 0 \\ \frac{d}{2} & 0 & -\frac{L_{eff}}{2} \\ 0 & \frac{L_{eff}}{2} & 0 \end{bmatrix} \quad (4.16)$$

Equation 4.11 may now be evaluated to find the compliance matrix of each leg. The leg compliance matrix is symmetric and found to be of the following form

$$C_{leg} = \begin{bmatrix} c_{11} & 0 & c_{13} & 0 & c_{15} & 0 \\ 0 & c_{22} & 0 & c_{24} & 0 & c_{26} \\ c_{13} & 0 & c_{33} & 0 & c_{35} & 0 \\ 0 & c_{24} & 0 & c_{44} & 0 & 0 \\ c_{15} & 0 & c_{35} & 0 & c_{55} & 0 \\ 0 & c_{26} & 0 & 0 & 0 & c_{66} \end{bmatrix} \quad (4.17)$$

where

$$\begin{aligned}
c_{11} &= 2C_{b1} + dC_{b5}, & c_{13} &= -\frac{L_{eff}d}{2}C_{b5}, & c_{15} &= dC_{b5} \\
c_{22} &= 2C_{b2} + \frac{L_{eff}^2}{2}C_{b6} + d^2C_{b4}, & c_{24} &= -dC_{b4}, & c_{26} &= L_{eff}C_{b6} \\
c_{33} &= 2\left(C_{b3} + \frac{L_{eff}^2}{4}C_{b5}\right), & c_{35} &= -L_{eff}C_{b5}, & c_{44} &= 2C_{b4} \\
c_{55} &= 2C_{b5}, & c_{66} &= 2C_{b6}, & & 
\end{aligned}$$

and  $C_{bi}$  is the  $i$ th diagonal element of  $C_b$  given in equation 4.7.

#### 4.1.3 Platform Compliance

The compliance matrix of the central platform can be found by summing the stiffness contribution of each leg and inverting the resulting matrix, details of this procedure are given in [31]. The expressions for the elements of the compliance matrix of the platform given by

$$C = \text{diag}[C_x \quad C_y \quad C_z \quad C_{\theta_x} \quad C_{\theta_y} \quad C_{\theta_z}] \quad (4.18)$$

that were published in [31] are modified by replacing  $L$  with  $L_{eff}$  to account for the compliance of the connector, the resulting expressions may be written as follows:

$$C_x = \frac{L_{eff}^3}{12EI_y} \left[ \frac{4\left(\frac{d}{b}\right)^2 + \frac{4}{3}}{3\left(\frac{d}{b}\right)^2 + \left(\frac{L_{eff}}{b}\right)^2 + 1} \right] \quad (4.19)$$

$$C_y = \frac{L_{eff}^3}{12EI_z} \left[ 2\left(\frac{EI_z}{GI_x}\right)\left(\frac{d}{L_{eff}}\right)^2 + \frac{2}{3} \right] \quad (4.20)$$

$$C_z = C_x \quad (4.21)$$

$$\begin{aligned}
&C_{\theta_x} \\
&= \frac{L_{eff}}{EI_z} \left\{ \frac{4\left(\frac{EI_z}{GI_x}\right)\left(\frac{d}{L_{eff}}\right)^2 + \frac{4}{3}}{\left[3\left(\frac{EI_z}{GI_x}\right) + 6\right]\left(\frac{d}{L_{eff}}\right)^2 + 12\left[\frac{nd}{L_{eff}^2} + \left(\frac{m}{L_{eff}}\right)^2 + \left(\frac{n}{L_{eff}}\right)^2 + \frac{m}{L_{eff}}\right] + 4 + \frac{GI_x}{EI_z}} \right\} \quad (4.22)
\end{aligned}$$

$$\begin{aligned}
&C_{\theta_y} \\
&= \frac{L_{eff}}{EI_y} \left\{ \frac{2\left(\frac{d}{b}\right)^2 + \frac{2}{3}}{3\left(\frac{L_{eff}}{b}\right)^2 \left\{ \left[12\left(\frac{m}{L_{eff}}\right)^2 + 12\left(\frac{m}{L_{eff}}\right) + 5\right]\left(\frac{d}{L_{eff}}\right)^2 + 4\left(\frac{nd}{L_{eff}^2}\right) + 4\left(\frac{n}{L_{eff}}\right)^2 \right\} + 12\left(\frac{m}{L_{eff}}\right)^2 + 12\left(\frac{m}{L_{eff}}\right) + 4} \right\} \quad (4.23)
\end{aligned}$$

$$C_{\theta_z} = C_{\theta_x} \quad (4.24)$$



These equations can be used for rapidly iterating through designs to obtain specified stiffnesses, which are the reciprocals of the compliances.

## 4.2 Stress Analysis

The stress at critical points of the orthoplanar spring will now be analyzed. In the following analysis, a displacement load in the sensor frame's y-axis will be applied to the central platform and the maximum stresses at the ends of each beam segment will be calculated. The force acting on the platform of the orthoplanar spring may be calculated for insight as well as a step towards finding stress, it is given by

$$F_y = \frac{\delta y}{C_y} \quad (4.25)$$

and the force acting on each leg of the orthoplanar spring is given by

$$F_{y,leg} = F_y/3 \quad (4.26)$$

Neglecting torsional stress, each beam segment of the orthoplanar spring is a fixed guided beam with a maximum bending stress given by

$$\sigma = \frac{3F_{y,leg}L_{eff}}{bh^2} = \frac{F_yL_{eff}}{bh^2} \quad (4.27)$$

A number of finite element simulations were performed on a cantilevered beam with a stress concentration similar to the beam segments of the orthoplanar spring and varying fillet radius, beam width, and beam thickness. Regressions to the finite element data result in expressions for the stress concentration factor which are given by

$$K_t = A \left( \frac{r}{b} \right)^c \quad (4.28)$$

$$A = -0.0161 \left( \frac{b}{h} \right) + 1.117 \quad (4.29)$$

$$c = -0.0043 \left( \frac{b}{h} \right) - 0.248 \quad (4.30)$$

where  $r$  is the fillet radius. The stress concentration data is given in Appendix B.

### 4.3 Finite Element Analysis Validation of Compliance and Stress Analysis

Linear finite element analysis simulations were run using SolidWorks to validate the stress and compliance analysis. Linearity allows the stiffness to be ascertained with a single force-displacement data point. Four finite element analyses were done using the design parameters given in Appendix C. The mesh, boundary conditions, and configuration of applied forces are shown in Figure 4.3 for the applied force case. There are two areas over which force was applied on the platform. It was ensured that the centroid of the combined areas lies at the centroid of the platform where the compliance matrix is diagonal, therefore no couples are applied when equal forces act in the same direction on these areas. Moments were generated on the platform by setting the forces acting on the two areas in opposite directions. A standard mesh was applied in SolidWorks with element sizes between 0.87 and 2.35 mm for all simulations.

The results of the simulations are shown in Table 4.1 and 4.2. It was found that the maximum stiffness error between the theoretical calculations and FEA was about 10% for both rotational and translational stiffnesses, the maximum Von Mises stress error was found to be 10% as well. A greater number of simulations may be done to better understand the accuracy of the theoretical model compared to FEA results, however, these preliminary findings suggest the theoretical calculations are adequate for early design iterations. Finite element analysis simulations should still be done on the final design.

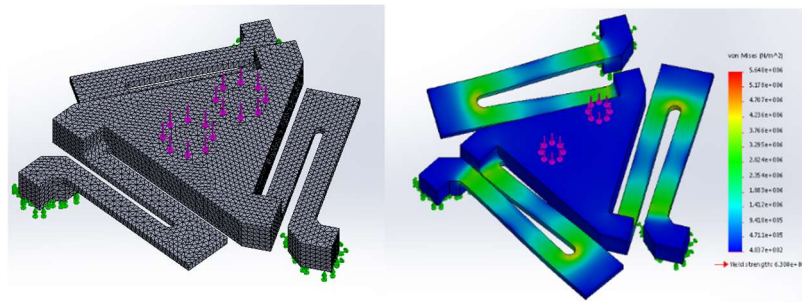


**Figure 4.3:** Setup and results of FEA with applied force.

**Table 4.1:** FEA and theoretically determined stiffnesses.

Design	Translational Stiffness ( $N/mm$ )		Rotational Stiffness ( $N \cdot mm/rad$ )	
	FEA	Theoretical	FEA	Theoretical
1	7.496	7.9956	9632.8	10178
2	5.920	6.5195	7110.6	7689.6
3	3.712	3.975	4410.27	4700.2
4	3.008	3.3159	3617.4	3915.0

**Table 4.2:** FEA and theoretically determined maximum Von Mises stresses.

Design	Max stress with Deflection of 4.7 mm (MPa)	
	FEA	Theoretical
1	32.5	29.4
2	29.7	29.8
3	19.7	22.1
4	47.8	45.6

#### 4.4 Mechanical Design Method

The mechanical design of the prototype consisted of specifying the dimensions and materials of all mechanical components including the orthoplanar spring, mechanical limits, base structure, and mounts. An iterative procedure was developed to design the orthoplanar spring and mechanical limits for specified stiffnesses, compactness, and measurement range. The base structure and mounts were designed around the transducer design as discussed in Chapter 5, and for compatibility with the robot on which the sensor is mounted.

##### 4.4.1 Orthoplanar Spring and Mechanical Limit Iterative Design Procedure

An iterative design procedure, shown in Figure 4.5, was used in the design the orthoplanar spring and mechanical limits. The iterative procedure begins with trial values for the orthoplanar spring design parameters listed in Table 4.3. A material is selected yielding  $E$ ,  $G$ ,  $S_y$ , and  $S_f$ , and trial values are selected for the beam geometry and location parameters. Connector width,  $w$ , has no part in the design procedure, however, it should be chosen large enough that the compliance of the connector is modeled correctly. Footprint size may be defined in many ways; however, the diameter of a circle which circumscribes the orthoplanar spring was used as a measure of footprint. For a wide range of design parameters, this diameter is given by

$$D = 2 \sqrt{(L + w + m)^2 + \left(n + d + \frac{1}{2}b\right)^2} \quad (4.31)$$

The next step in the procedure is to calculate the compliance matrix of the orthoplanar spring using equations 4.5 and 4.19 – 4.24. Note that in equation 4.5,  $c$  should be set equal to  $0.5(d - b)$ . If stiffness

and footprint requirements are not met, design parameters are modified using guidelines presented in section 4.4.2.

**Table 4.3:** Orthoplanar spring parameters.

Type of Parameters	Parameters
Material	$E, G, S_y, S_f$
Beam geometry	$b, L, h$
Beam location	$m, n, d, g$
Misc.	$w$

With a trial design of the orthoplanar spring established, the next step is to design the mechanical limits. The mechanical limits are designed to limit deflections of the orthoplanar spring so it is not overstressed. A layout of the mechanical limits is shown in Figure 4.4.

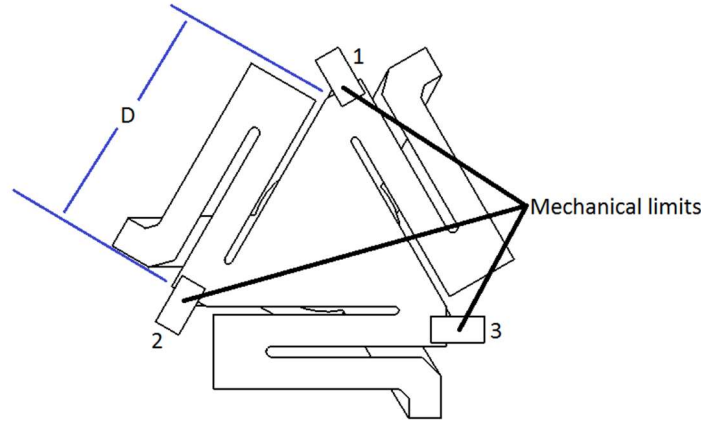


**Figure 4.4:** Mechanical limit layout with numbering.

The task of designing the mechanical limits is essentially the task of answering the question- how much deflection should be allowed at the points where the mechanical limits are installed? To answer this question, displacements of the platform must be transformed into displacements at points on the orthoplanar spring where mechanical limits are installed. For the case where the mechanical limits are located at the vertices of the triangular platform of the orthoplanar spring, this transformation is given by

$$\begin{bmatrix} \delta y_1 \\ \delta y_2 \\ \delta y_3 \end{bmatrix} = J_m^{-1} \begin{bmatrix} \delta y \\ \delta \theta_x \\ \delta \theta_y \end{bmatrix} \quad (4.32)$$

where

$$J_m^{-1} = \begin{bmatrix} 1 & -\frac{D}{\sqrt{3}} & 0 \\ 1 & \frac{D}{2\sqrt{3}} & \frac{D}{2} \\ 1 & \frac{D}{2\sqrt{3}} & -\frac{D}{2} \end{bmatrix} \quad (4.33)$$

and  $D$  is the distance between mechanical limits. The relationship between deflections at the mechanical limits and the forces and moments acting on the sensor is then given by

$$\begin{bmatrix} \delta y_1 \\ \delta y_2 \\ \delta y_3 \end{bmatrix} = J_m^{-1} C \begin{bmatrix} F_y \\ M_x \\ M_z \end{bmatrix} \quad (4.34)$$

where only platform displacements in the compliant degrees of freedom are considered, with the assumption that the other degrees-of-freedom are very stiff,  $C$  is therefore given by

$$C = \begin{bmatrix} C_y & 0 & 0 \\ 0 & C_{\theta x} & 0 \\ 0 & 0 & C_{\theta z} \end{bmatrix} \quad (4.35)$$

For mechanical limit design, the platform displacements  $[\delta y \quad \delta \theta_x \quad \delta \theta_y]^T$  should correspond to a specified maximum loading that can be measured by the sensor; loadings greater than this will cause interference with the mechanical limits. The measurement range requirements of the sensor may be written as

$$F_{yMin} < F_y < F_{yMax} \quad (4.36)$$

$$M_{xMin} < M_x < M_{xMax} \quad (4.37)$$

$$M_{zMin} < M_z < M_{zMax} \quad (4.38)$$

Now, the maximum and minimum deflections at the mechanical limit locations must be found under the range of loadings corresponding to the measurement range. For the case where the mechanical limits are located at the vertices of the orthoplanar spring platform, the forces and moments that result in the largest deflection at each mechanical limit are given by

$$F_{max,1} = [F_{yMax} \quad M_{xMin} \quad 0]^T \quad (4.39)$$

and

$$F_{min,1} = [F_{yMin} \quad M_{xMax} \quad 0]^T \quad (4.40)$$

for mechanical limit one;

$$F_{max,2} = [F_{yMax} \quad M_{xMax} \quad M_{zMax}]^T \quad (4.41)$$

and

$$F_{min,2} = [F_{yMin} \quad M_{xMin} \quad M_{zMin}]^T \quad (4.42)$$

for mechanical limit 2; and

$$F_{max,2} = [F_{yMax} \quad M_{xMax} \quad M_{zMax}]^T \quad (4.43)$$

and

$$F_{min,3} = [F_{yMin} \quad M_{xMin} \quad M_{zMax}]^T \quad (4.44)$$

for mechanical limit 3, where  $F_{max,i}$  and  $F_{min,i}$  are the force/moment vectors causing the maximum and minimum deflections at mechanical limit  $i$  using the numbering scheme in Figure 4.4.

The force-moment vectors expressed in equations 4.39 – 4.44 are then inserted into equation 4.34 to find the maximum and minimum deflections at each mechanical limit; this procedure can be expressed as

$$\delta_{max,k} = row_k(J_m^{-1}C)F_{max,k} \quad (4.45)$$

and

$$\delta_{min,k} = row_k(J_m^{-1}C)F_{min,k} \quad (4.46)$$

It is desirable to have each mechanical limit be the same design, therefore, each must allow the deflection range  $R$ , given by

$$R \geq \max(\delta_{max,1}, \delta_{max,2}, \delta_{max,3}) - \min(\delta_{min,1}, \delta_{min,2}, \delta_{min,3}) + t \quad (4.47)$$

where  $t$  is the thickness of the orthoplanar spring.  $R$  may be chosen larger than the right-hand-side of inequality 4.61 to allow for compliance of the sensor past its measurement range; this may be desirable to reduce impact forces; however, the maximum possible stress will be increased.

The mechanical limit design is followed by the calculation of stresses. The maximum stress will occur when a force is applied to the sensor causing all of the mechanical limits to be reached. The platform displacement vector causing maximum stress is thus given by

$$\delta y = \max(\delta_{max,1}, \delta_{max,2}, \delta_{max,3}, -\delta_{min,1}, -\delta_{min,2}, -\delta_{min,3}) + e \quad (4.48)$$

where  $e$  is the allowed deflections past the measurement range. This displacement is input to the stress analysis in section 4.2 and checked against the yield strength or fatigue strength of the material. If the stress is too high, the trial parameters are modified as described in the next section to reduce the stress.

#### 4.4.2 Guidelines for Trial Parameter Selection

During the iterative design process described above, trial parameters had to be re-selected between iterations to progress the design to meet design requirements. Because the orthoplanar spring is composed of beam elements, a single beam element is analyzed to provide insight for selecting trial parameters. A cantilevered beam, as shown in Figure 4.6, is acted on by a force at its free end. Using Euler-Bernoulli beam theory, the maximum stress in this beam is given by

$$\sigma_{max} = \frac{6FL}{bh^2} \quad (4.49)$$

The deflection of the beam's free-end is given by

$$\delta = \frac{4FL^3}{Ebh^3} \quad (4.50)$$

and the beam's stiffness is given by

$$K = \frac{Ebh^3}{4L^3} \quad (4.51)$$

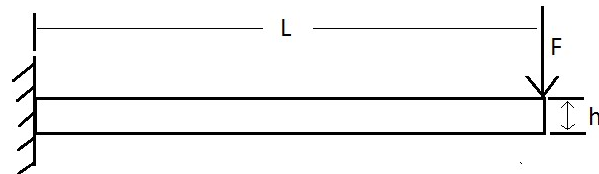


**Figure 4.5:** Cantilevered beam with force at free end.

The compactness of the orthoplanar spring is typically sensitive to beam length, thus the single beam analog to compactness was taken as beam length,  $L$ . Furthermore, beam stiffness and maximum stress

are directly analogous to orthoplanar spring stiffness and maximum stress. The above equations can be used to make decisions on how to modify the design parameters of the orthoplanar spring form iteration to iteration. The following observations regarding the above formula were found to be useful during the iterative process:

1. Equation 4.51 indicates stiffness is much more sensitive to  $h$  and  $L$  compared to  $b$ .
2. Equations 4.49 and 4.51 can be combined to obtain

$$\sigma_{max} = \frac{3}{2}FE \frac{h}{KL^2} \quad (4.52)$$

indicating the maximum stress, stiffness, and material may be kept constant while changing the footprint of the orthoplanar spring if the ratio between  $h$  and  $L^2$  is kept constant and  $b$  is given by

$$b = \frac{4K}{E} \left(\frac{L}{h}\right)^3 \quad (4.53)$$

Stress may also be reduced by reducing the ratio between  $h$  and  $L^2$ .

3. Equation 4.52 indicates that if the material strength to modulus ratio is increased,  $L$  may be reduced, possibly resulting in a smaller footprint.

#### 4.4.3 Base Structure and Mounting Component Design

The prototype's base structure and mounting components were designed after the transducer design presented in Chapter 5 was carried out. The base structure was designed to place the orthoplanar spring properly in the mechanical limits and place the Hall-effect sensor and magnets properly relative to one another as determined by the methods presented in Chapter 5. The based structure and mounting components should also be made stiff and compact, while allowing room for mounting wires. Grooves should be added to accommodate the Hall-effect sensors as well as aid in assembly as suggested in [25]. Finally, the mounting components are designed to accommodate the robot and end-effectors on which the sensor is to be implemented.



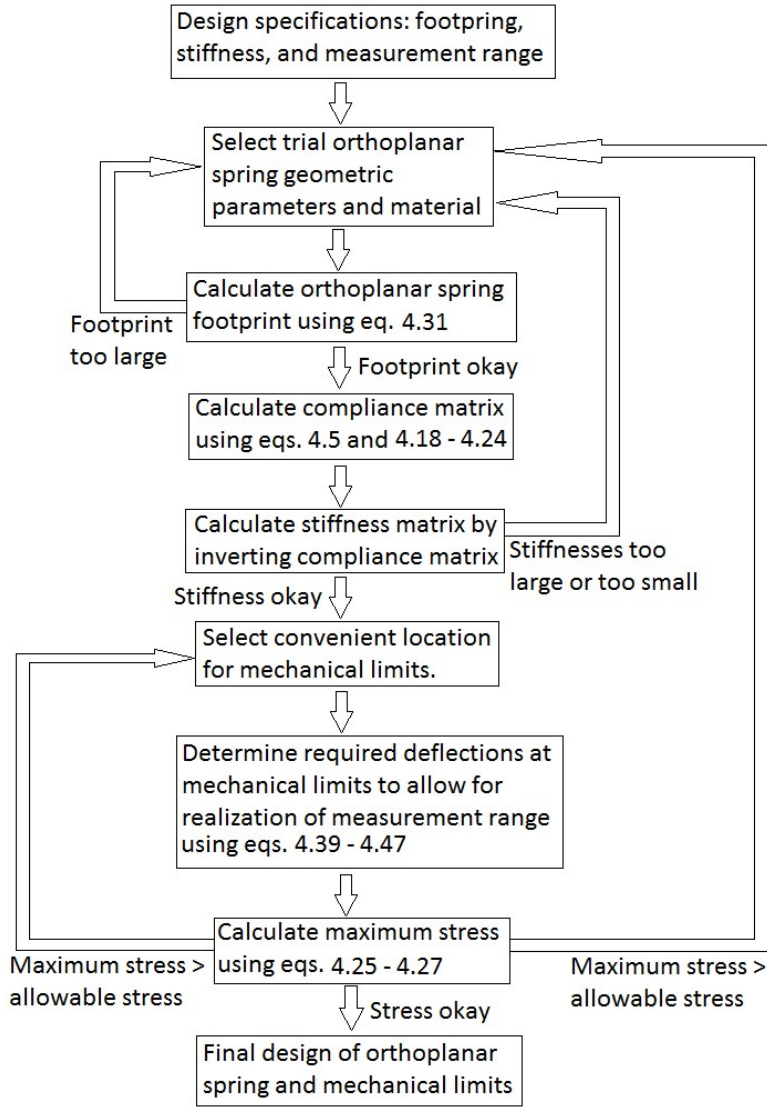


**Figure 4.6:** Iterative design procedure for orthoplanar spring and mechanical limits design.

## Chapter 5: Three-Axis Hall-effect Transducer Modeling and Design

This chapter presents a model of the developed force/torque sensor used for transducer design. The sensor includes three Hall-effect sensor-magnet pairs which are used to measure three components of force and torque. Hall-effect sensors respond to the magnetic field component perpendicular to the sensing element. Magnets mounted in the platform of the orthoplanar spring undergo displacements when forces and moments are applied. Hall-effect sensors installed on the base structure below the magnets are then able to sense these displacements via the associated change in magnetic fields at the Hall-effect sensors. Transducer design is considered to include the selection and placement of Hall-effect sensors and corresponding magnets. The model was also used in calibration laws introduced in Chapter 8. The following sections will mathematically model the motion of the magnets, the magnetic field acting on the Hall-effect sensors, and Hall-effect sensor response to the magnetic field. A transducer design procedure based on the developed mathematical model is then introduced.

### 5.1 Kinematics and Statics

To obtain the displacement vector from three single degree-of-freedom displacement sensors, the kinematics relating platform displacement to magnet deflections must be analyzed. It is assumed only small displacements occur and displacements occur only in the compliant degrees-of-freedom of the orthoplanar spring. The arrangement of the three magnets and Hall-effect sensors is shown in Figure 5.1. The kinematics can be analyzed by considering the magnet deflections resulting from  $\delta y$ ,  $\delta\theta_x$ , and  $\delta\theta_z$  individually, then summing the contribution from each degree-of-freedom of the platform. The resulting equations can be written in a matrix form given by

$$\begin{bmatrix} \delta y_1 \\ \delta y_2 \\ \delta y_3 \end{bmatrix} = J^{-1} \begin{bmatrix} \delta y \\ \delta\theta_x \\ \delta\theta_z \end{bmatrix} \quad (5.1)$$

where

$$J^{-1} = \begin{bmatrix} 1 & -\frac{s}{\sqrt{3}} & 0 \\ 1 & \frac{s}{2\sqrt{3}} & \frac{s}{2} \\ 1 & \frac{s}{2\sqrt{3}} & -\frac{s}{2} \end{bmatrix} \quad (5.2)$$

and  $[\delta y_1 \ \delta y_2 \ \delta y_3]^T$  is the vector of magnet displacements, and  $[\delta y \ \delta \theta_x \ \delta \theta_y]^T$  is the platform displacement vector in the compliant degrees-of-freedom referring to the frame shown in Figure 5.1a. The first column of  $J^{-1}$  contains ones because translation of the platform along the y-axis only by  $\delta y$  yields deflections of each magnet of  $\delta y$ . The elements of the second and third columns of  $J^{-1}$  correspond to the distance each magnet is from the x and z-axis respectively, these elements are given by

$$J^{-1}_{i2} = -z\text{-coordinate of magnet } i$$

$$J^{-1}_{i3} = x\text{-coordinate of magnet } i$$

The forces acting on the sensor are then related to the magnet displacements by

$$\begin{bmatrix} \delta y_1 \\ \delta y_2 \\ \delta y_3 \end{bmatrix} = J^{-1} C \begin{bmatrix} F_y \\ M_x \\ M_z \end{bmatrix} \quad (5.3)$$

where  $C$  is the compliance matrix of the platform in the compliant degrees-of-freedom only, given by

$$C = \begin{bmatrix} C_y & 0 & 0 \\ 0 & C_{\theta_x} & 0 \\ 0 & 0 & C_{\theta_z} \end{bmatrix} \quad (5.4)$$

These equations are similar to those used in the design of the mechanical limits presented in Chapter 4.

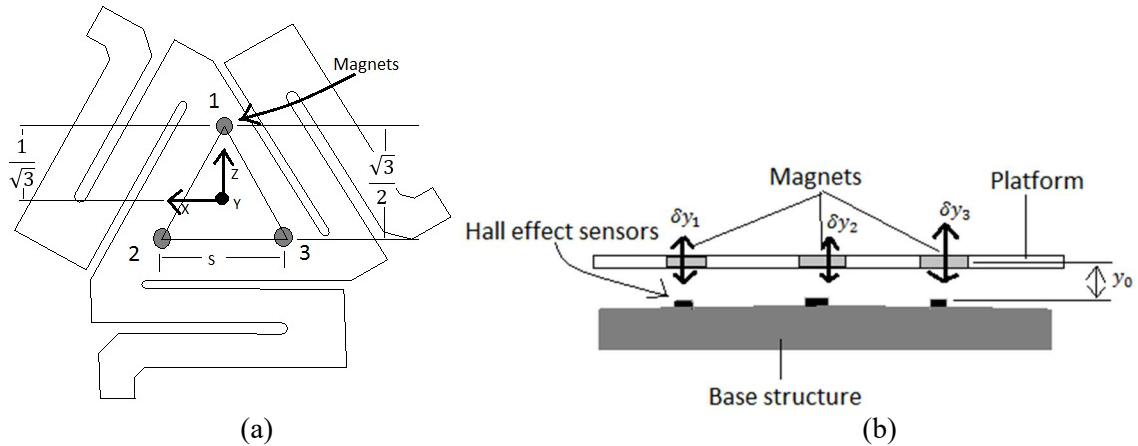


**Figure 5.1:** General layout of magnets and Hall-effect sensors, (a) overhead view, (b) side view.

## 5.2 Magnetic Field Model

To determine a suitable combination of Hall-effect sensor sensitivity, magnet size and strength, and Hall-effect sensor and magnet placement, the magnetic field of a magnet is now analyzed. Electromagnetic theory allows for the calculation of the magnetic field distribution caused by electric currents; a simple model of the magnetic field produced by a thin cylindrical permanent magnet can be found by approximating the magnet as a circular current loop. If it is assumed that the Hall-effect sensor is located on the symmetry axis of the cylindrical magnet, the magnetic field vector will be along the magnets axis and have a strength given by

$$B = \frac{1}{2} \frac{\mu I R^2}{(y^2 + R^2)^{\frac{3}{2}}} \quad (5.5)$$

where  $\mu$ ,  $R$ , and  $I$  are the magnetic permeability, radius of the current loop, and current of the current loop and  $y$  is the position of the Hall-effect sensor along the axis of the magnet. For convenience,  $\frac{1}{2} \mu I R^2$  will be combined into a single constant  $a$ , given by

$$a = \frac{1}{2} \mu I R^2 \quad (5.6)$$

To use the magnetic field model in the design stage,  $a$  must be determined from the specifications of the magnet. The value of  $a$  depends on the magnets dimensions and remanence of the magnet's material. To compute  $a$ , the dimensions and remanence of the magnet can be used to calculate the surface field strength on the symmetry axis of the magnet by [45]

$$B_{surf} = \frac{B_r}{2} \frac{t}{\sqrt{R^2 + t^2}} \quad (5.8)$$

where  $B_r$  is the magnetic remanence,  $t$  is the magnet's thickness, and  $R$  is now taken as the radius of the magnet. The value of  $a$  can then be found by setting  $B = B_{surf}$  and  $y = t/2$  in equation 5.5 and solving for  $a$ . The resulting expression for  $a$  is given by

$$a = \frac{B_r}{2} \frac{t}{\sqrt{R^2 + t^2}} \left[ \left( \frac{t}{2} \right)^2 + R^2 \right]^{\frac{3}{2}} \quad (5.9)$$

Because the magnet is approximated by a single current loop, this formula is only valid when the thickness of the magnet is small compared to the diameter.

### 5.3 Hall-effect Sensor Response

Hall-effect sensors have many operating characteristics including: supply voltage and current, saturation voltage, static sensitivity, quiescent voltage output, temperature sensitivity, hysteresis, linearity, noise, drift etc. While it is important to select a Hall-effect sensor based a variety of operating characteristics, this thesis deals with selecting characteristics that are most pertinent to force/torque sensing, namely sensitivity, quiescent voltage output, and saturation voltage. These are the characteristics that determine the Hall-effect sensor's nominal output response to a magnetic field, shown in Figure 5.2.

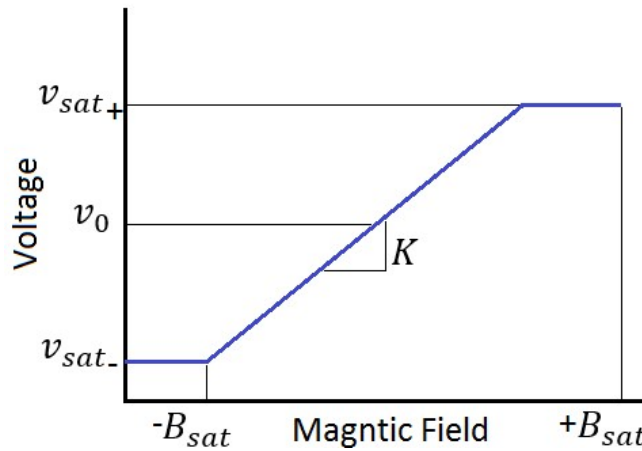


**Figure 5.2:** Nominal Hall-effect sensor voltage output in response to magnetic field.

The sensitivity, quiescent output voltage, and saturation voltages of the Hall-effect sensor determine the range of magnetic field strengths that can be sensed. This maximum field strength that can be sensed is given by

$$B_{sat} = \frac{|v_{sat} - v_0|}{K} \quad (5.10)$$

where

$B_{sat}$  = Maximum or saturation magnetic field strength

$v_{sat}$  = Saturation voltage

$v_0$  = Quiescent voltage

$K =$  Static sensitivity

and the static sensitivity is given by

$$K = \frac{dv}{dB} \quad (5.11)$$

For many Hall-effect sensors,  $v_{sat}$  and  $v_0$  are nearly equal to the supply voltage and one half the supply voltage respectively.

#### 5.4 Hall-effect Sensor and Magnet Selection and Placement

The previous three sections have discussed the relationship between applied forces and magnet displacements, the relationship between magnet displacements and magnetic field strength at the Hall-effect sensors, and the response of the Hall-effect sensors to the magnetic field. The result of this is an approximate model of the force/torque sensor that can be used to select components and determine where to mount them on the structure of the force/torque sensor.

The parameters that must be specified to complete the design of the sensing system are listed in Table 5.1. An iterative design procedure used to select the final design values for these parameters begins with selecting a trial Hall-effect sensor and magnet; this yields trial values for  $K$ ,  $v_0$ ,  $v_{sat}$ ,  $t$ ,  $D$ , and  $B_r$ . The magnetic field strength that causes Hall-effect sensor saturation is given by equation 5.10. The Hall-effect sensor-magnet separation distance when the Hall-effect sensor saturates is then calculated by

$$y_{sat} = \sqrt{\left(\frac{a}{B_{sat}}\right)^{\frac{2}{3}} - R^2} \quad (5.13)$$

where  $R$  is the radius of the magnet. The force and moment measurement range requirements and orthoplanar spring compliance values are then used to find the minimum and maximum deflections experienced by the magnets as a function of magnet separation,  $s$ , shown in Figure 5.1. Formulae identical to those used in Chapter 4 to design the mechanical limits are used to find the minimum and maximum deflections of the magnets- these formula are repeated here for convenience. The loadings resulting in maximum and minimum deflections of each magnet are given by

$$F_{max,1} = [F_{yMax} \quad M_{xMin} \quad 0]^T \quad (5.14)$$

and

$$F_{min,1} = [F_{yMin} \quad M_{xMax} \quad 0]^T \quad (5.15)$$

for magnet 1,

$$F_{max,2} = [F_{yMax} \quad M_{xMax} \quad M_{zMax}]^T \quad (5.16)$$

and

$$F_{min,2} = [F_{yMin} \quad M_{xMin} \quad M_{zMin}]^T \quad (5.17)$$

for magnet 2, and

$$F_{max,2} = [F_{yMax} \quad M_{xMax} \quad M_{zMax}]^T \quad (5.18)$$

and

$$F_{min,3} = [F_{yMin} \quad M_{xMin} \quad M_{zMax}]^T \quad (5.19)$$

for magnet 3, where  $F_{max,i}$  and  $F_{min,i}$  are the force/moment vectors causing the maximum and minimum deflections at magnet  $i$  using the numbering scheme shown in Figure 5.1.

The force-moment vectors given in equations 5.14 – 5.19 are then inserted into equation 5.3 to find the maximum and minimum deflections at each magnet; this procedure can be expressed as

$$\delta_{max,k} = row_k(J^{-1}C)F_{max,k} \quad (5.20)$$

and

$$\delta_{min,k} = row_k(J^{-1}C)F_{min,k} \quad (5.21)$$

The undeflected Hall-effect sensor-magnet separation required to avoid Hall-effect sensor saturation can be found by

$$y_o = -\max(\delta_{min,1}, \delta_{min,2}, \delta_{min,3}) + y_{sat} \quad (5.22)$$

The maximum Hall-effect sensor-magnet separation is then given by

$$y_{i,max} = y_o + \delta y_{i,max}, \quad i = 1,2,3 \quad (5.23)$$

**Table 5.1:** Transducer design parameters.

Placement parameters	$s, y_0$
Magnet parameters	$t, R, B_r$
Hall-effect sensor parameters	$K, v_0, v_{sat}$

The resolution of the force/torque sensor is reduced as the Hall-effect sensor-magnet distance increases. This is because the magnetic field strength changes very little as it approaches zero at large distances, thereby amplifying voltage errors. The distance versus magnetic field strength derivative may be found from equation 5.5 and 5.6 at maximum Hall-effect sensor magnet separation and is given by

$$\frac{dy_i}{dB} = -\frac{(y_{i,max}^2 + R^2)^{\frac{5}{2}}}{3ay_{i,max}} \quad (5.24)$$

Voltage errors are propagated into force and moment errors by the square root of the sum of the squares of the individual Hall-effect sensor errors, this root-sum-squares may be written as

$$\delta F_k = \frac{\delta V}{K} \sqrt{\sum_{j=1}^3 \left\{ [C^{-1}J]_{kj}^2 \left( \frac{dy_j}{dB} \right)^2 \right\}} \quad (5.25)$$

where  $\delta V$  is the voltage measurement resolution and  $\delta F_k$  is the  $k$ th component of the vector given by

$$\delta F = [\delta F_y \quad \delta M_x \quad \delta M_z]^T \quad (5.26)$$

With the Hall-effect sensor and magnet chosen,  $\delta F$  is a function of only  $s$ . It is desirable to find  $s$  that minimizes the force error  $\delta F$ . Because  $\delta F$  has three components, an optimization criterion is needed to minimize  $\delta F$  in some sense. The optimization criteria chosen in this thesis is the minimization of the root sum of squares of the relative errors in each measurement axis, given by

$$\min \left\{ \sqrt{\left( \frac{\delta F_y}{F_{yMax}} \right)^2 + \left( \frac{\delta M_x}{M_{xMax}} \right)^2 + \left( \frac{\delta M_z}{M_{zMax}} \right)^2} \right\} \quad (5.27)$$

Aside from what has been modeled in the above sections, there are other important considerations to be made when selecting and determining the placement of Hall-effect sensors and magnets. First,  $s$  should be large enough and  $R$  should be small enough that the magnets do not interfere with one another, this should be the case if  $s$  is several times  $R$ . It should also be ensured that the magnets fit on the platform



of the orthoplanar spring. Next, the magnets should have a large enough diameter such that the design is not overly sensitive to assembly errors in the placement of magnets and Hall-effect sensors, therefore magnet diameter should be much greater than the expected assembly error.

## Chapter 6: Prototype Design and Construction

A prototype was developed to test the validity of the design concept and the design calculations presented in chapters 4 and 5. The details of the prototype's design and construction are presented in this chapter. Matlab scripts and functions were created which implement the design equations presented in chapters 4 and 5; iterations were performed until a design meeting the desired measurement range, stiffness, and footprint was obtained. SolidWorks was used to create solid models of the design and perform FEA simulations. The finalized design was then produced by rapid prototyping its components using 3-D printing and laser cutting; the components were then assembled with adhesive. The prototype described in this chapter was calibrated and underwent testing as presented in chapters 7 and 8.

### 6.1 Prototype Design Specifications

The measurement range specification was determined by the payload and desired force control capabilities of the robot. For this research, the robot was to support a moment of 0.5 kg at 100 mm and a force of 5 N during force control. The measurement range requirements were evaluated by equations 3.1 and 3.2 as follows:

$$F_{meas} \geq F_{env} + mg = 5 + 0.5 \times 9.8 = 9.9 \text{ N} \quad (6.1)$$

and

$$M_{meas} \geq mgr_{cg} = 0.5 \times 9.8 \times 100 \text{ N} \cdot \text{mm} = 490 \text{ N} \cdot \text{mm} \quad (6.2)$$

The measurement ranges selected are listed in Table 6.1.

**Table 6.1:** Sensor measurement ranges.

Measurement Axis	Measurement Range
$F_y$	-10: 10 N
$M_x$	-500: 500 N · mm
$M_z$	-500: 500 N · mm

The stiffness of the sensor was selected to have a high enough natural frequency when coupled with the end-effector and payload inertia. The sensor-inertia system is modeled as shown in Figure 6.1. A mass of 0.5 Kg is rigidly attached to the sensor at 100 mm. This model will yield conservative estimates for the systems eigenfrequencies. In this case the mass matrix and stiffness matrix are diagonal and equation 3.5 reduces to

$$\omega_t = \sqrt{\frac{K_y}{m}} \quad (6.3)$$

and

$$\omega_r = \sqrt{\frac{K_r}{I}} \quad (6.4)$$

where  $\omega_t$  and  $\omega_r$  are the natural frequencies of the system's rotational and translational modes respectively;  $K_y$  and  $K_r$  are the translational and rotational stiffness of the orthoplanar spring; and  $m$  and  $I$  are the mass and moment of inertia of the attached inertia. The moment of inertia of this system is given by

$$I = ml^2 = 0.5 \times 0.1^2 = 0.005 \text{ Kg} \cdot \text{m}^2 \quad (6.5)$$

In this research, the minimum natural frequency allowable was 5 Hz. Finally, it was desired to keep sensor displacements below 5 mm and 0.1 radians for expected loads. The final design stiffness values as calculated by equations 4.19 – 4.24, the resulting natural frequencies as determined by equation 6.3 and 6.4, and the maximum sensor displacements are listed in Table 6.2. The design stiffnesses satisfy the natural frequency and maximum displacement requirements. A stiffer sensor is typically better for position control, however, stiffness was kept low because of the benefits of compliance in force control.

**Table 6.2:** Sensor design stiffness, natural frequency, and maximum displacement.

Mode	Stiffness	Natural Frequency	Maximum Displacement
Translational	7.996 N/mm	20.2 Hz	1.24 mm
Rotational	10178 N · mm/rad	7.23 Hz	0.049 rad

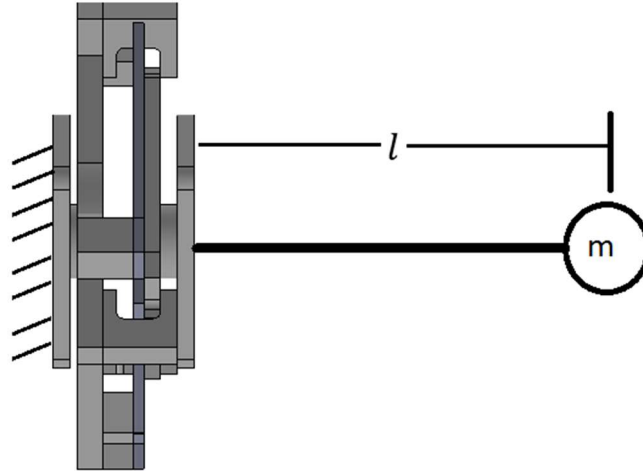


**Figure 6.1:** Sensor-inertia model.

It was ensured that the sensor's footprint was less than 150 mm. It was found that increasing the rotational stiffness while keeping translational stiffness constant tended to result in a larger footprint. However, a smaller footprint can generally be obtained with an overall stiffer sensor.

## 6.2 Prototype Design

The developed prototype is shown in Figure 6.2. The device consists of a lower mount, which is to be attached to the end of a robot arm, and an upper mount to be attached to an end-effector as shown in Figure 6.3. The mounts are designed to be fastened to the Wheelchair Mounted Robotic Arm (WMRA) and end-effector used in force control experiments discussed in Chapter 8. The other end of the lower mount is attached to the base structure. The outer ends of each leg of the orthoplanar spring are held fixed to the base structure with adhesive as indicated in Figure 6.2. A stiffener plate is attached on top of the orthoplanar spring platform to increase its stiffness and to allow for mounting the gripper. Magnets are mounted in holes in the central platform of the orthoplanar spring, and Hall-effect sensors are fixed to the base structure below the magnets as shown in Figure 6.4. The overall dimensions of the sensor are shown in Figure 6.5.

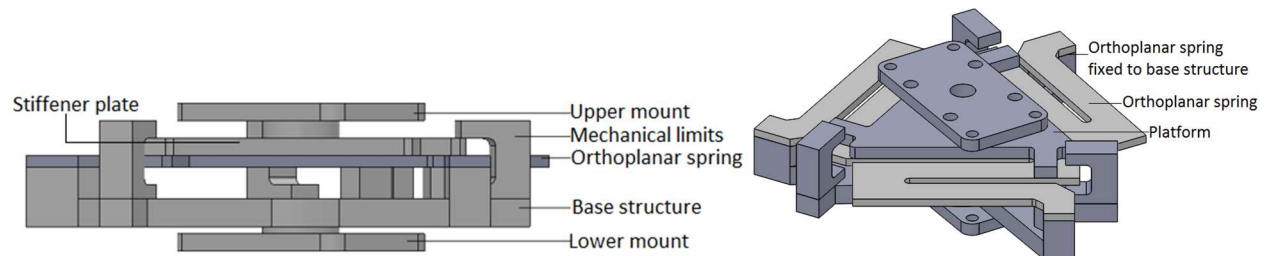


**Figure 6.2:** Mechanical design of sensor.

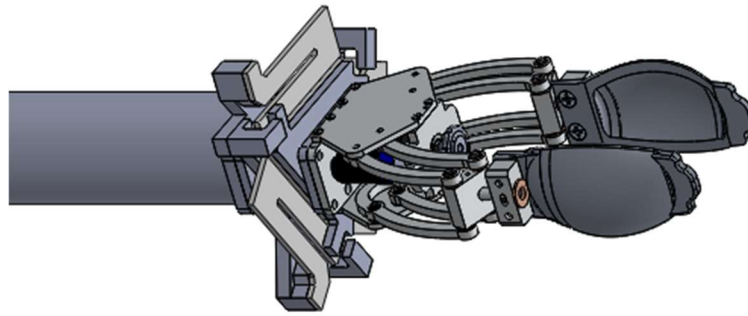


**Figure 6.3:** Rendering of compliant force/torque sensor integrated in robotic manipulator.

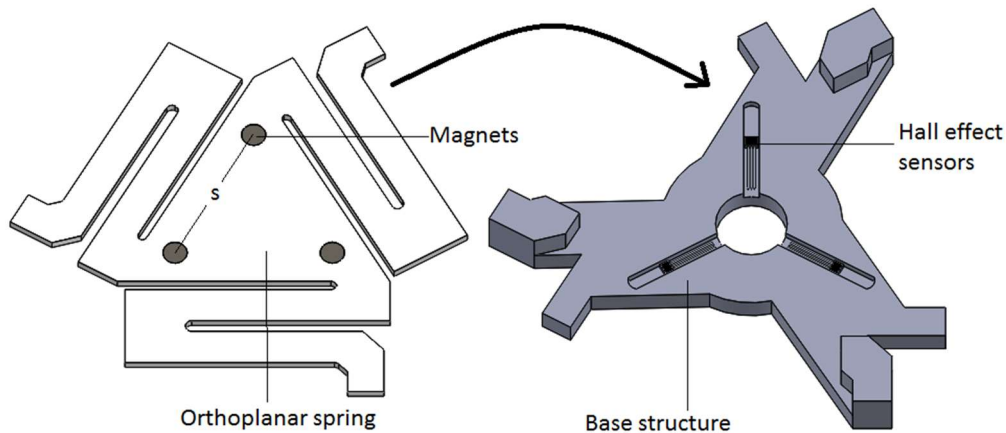


**Figure 6.4:** Transducer design of sensor.

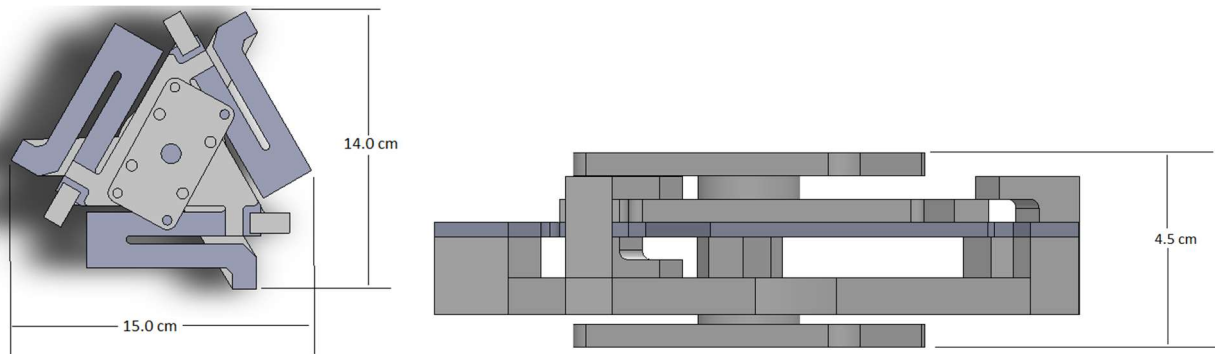


**Figure 6.5:** Overall dimensions of sensor.

### 6.2.1 Orthoplanar Spring Design and Fabrication

The orthoplanar spring was laser cut from Delrin, or acetal homopolymer sheet. Delrin was chosen because of its high strength, low elastic modulus, ductility, and good fatigue and creep characteristics. The typical material properties of Delrin listed in [39] are shown in Table 6.3 along with the design geometric parameters of the orthoplanar spring. As is often the case with polymers, the flexural modulus, flexural

yield strength, and flexural fatigue endurance limit for Delrin were given. The geometric parameters in Table 6.3 were defined in Figure 4.2. Following the design procedure in Chapter 4, the footprint and compliance matrix of the final design were calculated by equations 4.31 and 4.19 – 4.24 respectively; the results are shown in Table 6.4. To verify the analytical compliance and stress calculations, FEA was performed on the final design. The results of the finite element analysis and their comparison with the analytical calculations are shown in Table 6.5. It was found that close agreement was obtained between FEA results and analytical calculations. The full geometric stress concentration was applied to the analytically determined stress for comparison with finite element results. The calculated static failure safety factor for the prototype was 5.7, this is a relatively large safety factor and a long fatigue life is expected. Furthermore, it is unlikely the orthoplanar spring will be compressed to its maximum stress position very often. Data on the notch sensitivity and fatigue strength correction factors of Delrin polymer was not available, therefore fatigue life analysis was not performed.

**Table 6.3:** Orthoplanar spring design parameters.

Material Properties	Typical Value
Flexural Modulus, $E$	2900 MPa
Poisson Ratio, $\nu$	0.35
Flexural Yield Strength, $S_y$	99 MPa
Flexural Fatigue Endurance Limit, $S_f$	32 MPa
Geometric Parameters	Design Value
b	12 mm
L	50 mm
h	3.175 mm
m	-27.5 mm
n	35 mm
d	16 mm
w	20 mm
g	3 mm

**Table 6.4:** Footprint and compliance calculation results.

Parameter	Value
Footprint, $D$	15 cm
Compliance Matrix, $C$ ( $\frac{mm}{N}, \frac{rad}{N\cdot mm}$ )	$\begin{bmatrix} 0.0033 & 0 & 0 & 0 & 0 & 0 \\ 0 & 0.1251 & 0 & 0 & 0 & 0 \\ 0 & 0 & 0.0033 & 0 & 0 & 0 \\ 0 & 0 & 0 & 9.825 \times 10^{-5} & 0 & 0 \\ 0 & 0 & 0 & 0 & 1.108 \times 10^{-6} & 0 \\ 0 & 0 & 0 & 0 & 0 & 9.825 \times 10^{-5} \end{bmatrix}$

**Table 6.5:** Comparison of FEA results and design calculations for the final prototype design.

Parameter	FEA Result	Design Calculation
Translational stiffness ( $\frac{N}{mm}$ )	7.496	7.9956
Rotational stiffness ( $N \cdot \frac{mm}{rad}$ )	9633	1018
Maximum stress (MPa)	32.5	29.4

### 6.2.2 Mechanical Limits: Design and Fabrication

Mechanical limits were placed at each leg of the orthoplanar spring near the vertices of the orthoplanar spring platform as shown in Figure 6.6a. Equations 4.33 – 4.46 were used to find the range of deflections the mechanical limits must allow for the specified measurement ranges. It was found that a range of motion of 9.37 mm at each mechanical limit is required to allow for the full measurement range. Equation 4.47 was then used to select the key dimension of the mechanical limit,  $R$ . It was found that  $R > 12.6 \text{ mm}$  was required, therefore the mechanical limits were made with  $R = 13 \text{ mm}$ ; as shown in figure 6.6b. The mechanical limits were fabricated by 3-D printer using PLA plastic.

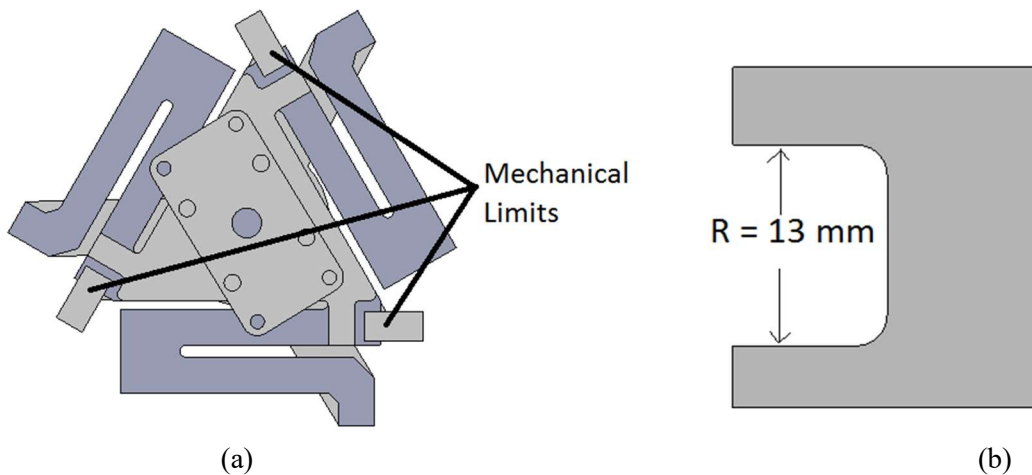


**Figure 6.6:** (a) Mechanical limit placement and design (b) mechanical limit itself.

### 6.2.3 Base Structure and Mounting Components: Design and Fabrication

The base structure has three main features: areas for mounting mechanical limits and the orthoplanar spring, grooves for the Hall-effect sensors, and a mounting point for the lower mount which connects the device to the robot. The base structure is shown in Figure 6.7a. The upper and lower mounts are designed to interface with the robot and gripper respectively. In the current prototype, the upper and

lower mounts are identical and are shown in Figure 6.7b. The base structure and mounts were 3-D printed using PLA plastic.

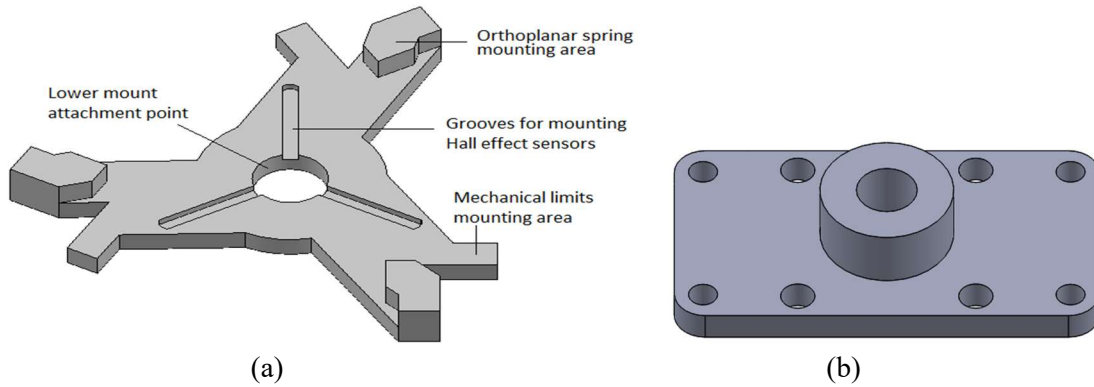


**Figure 6.7:** 3D models of (a) the base structure and (b) upper and lower mount.

### 6.2.4 Transducer Design

The transducer design includes the selection of Hall-effect sensors and magnets and their placement within the force/torque sensor. The selected Hall-effect sensors have a linear output with a sensitivity of 5 mV/G, a quiescent output voltage of 2.5 V, and saturation output voltages of 0.3 V and 4.7 V in the worst case according to the sensor's datasheet. Transducer design parameters are shown in Table 6.6. Other properties of the selected Hall-effect sensors include: temperature compensation, low impedance output, internal amplifier, and a dynamic offset cancelation feature. The Hall-effect sensor is in the form of an integrated circuit as shown in Figure 6.8a.

The magnets selected are neodymium with a rating between N35 and N45. This is an industry standard rating and implies a magnetic remanence between 11700 and 13700 G [40]; for design purposes, a value of 12700 G was assumed. The magnets are 3 mm thick and 8 mm in diameter as shown in Figure 6.8b. With these magnets paired with the selected Hall-effect sensors, the design equations presented in Chapter 5 indicated  $y_0 = 10.6 \text{ mm}$ , therefore the sensor was designed to place the magnet at approximately 10.6 mm when the orthoplanar spring is undeflected. The value of  $s$  that minimizes the effect of voltage errors on force and moment errors based on the optimization criterion given by equation 5.27 is  $s = 41 \text{ mm}$ . The optimization criterion is plotted against  $s$  in Figure 6.9. Near the optimum value there is very little



change in the optimization criterion- the prototype was designed with a suboptimal value of  $s = 52 \text{ mm}$  to allow more room for wiring, the optimization criterion to be minimized increased by just 2.8%.

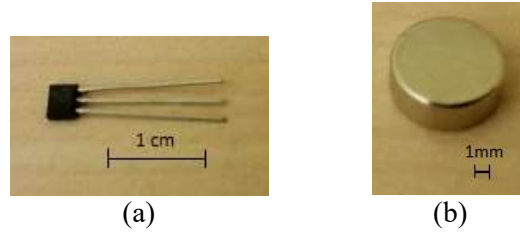


**Figure 6.8:** (a) Hall-effect sensor and (b) magnet used in prototype.

**Table 6.6:** Transducer design parameters.

Hall-effect sensor parameters	
K	5 mV/G
$v_0$	2.5 V
$v_{\text{sat}}$	0.3 V, 4.7 V
Magnet Parameters	
t	3 mm
D	8mm
$B_r$	12700 G
Placement Parameters	
$y_0$	$\cong 10.6 \text{ mm}$
s	52 mm

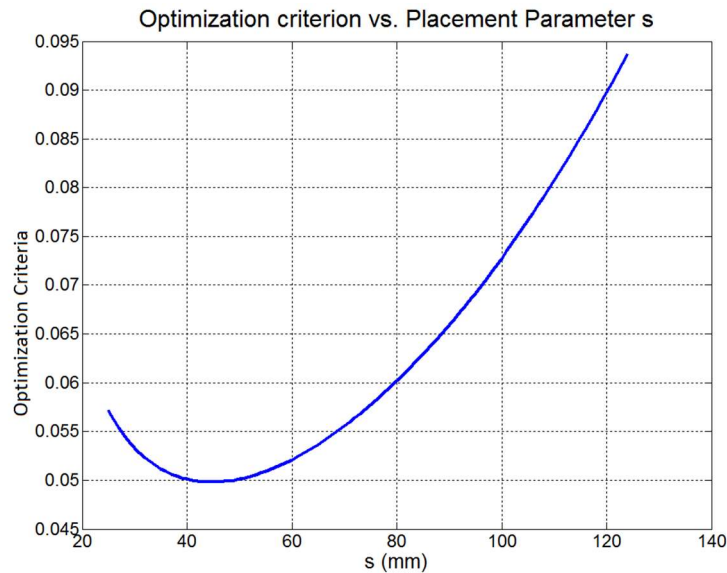


**Figure 6.9:** Plot of the optimization criterion given by equation 5.27 vs. the placement parameter  $s$ .

### 6.3 Prototype Assembly

After each of the components discussed in the previous section were fabricated, the prototype was assembled using J-B Weld epoxy. Each of the fabricated components is shown in Figure 6.10a and the

assembled prototype is shown in Figure 6.10b. During the assembly of the prototype, steps were taken to ensure alignment of the Hall-effect sensors and magnets. The assembly procedure was as follows:

1. The orthoplanar spring was placed on the base structure and markings were made on the base structure where the Hall-effect sensors were to be mounted.
2. The magnets were mounted in orthoplanar spring and the stiffener plate was epoxied in place.
3. Hall-effect sensor wires and Hall-effect sensors were integrated and epoxied on the base structure.
4. The epoxy was given time to dry overnight
5. The hardware was setup to read voltages from the Hall-effect sensors
6. The orthoplanar spring, stiffener plate, and magnets sub-assembly were epoxied onto the base structure while reading Hall-effect sensor voltages. Final placement was found when each Hall-effect sensor read a maximum change in voltage and all Hall-effect sensor voltages were nearly the same.
7. Epoxy was given time to dry overnight
8. The mounts and mechanical limits were epoxied in place

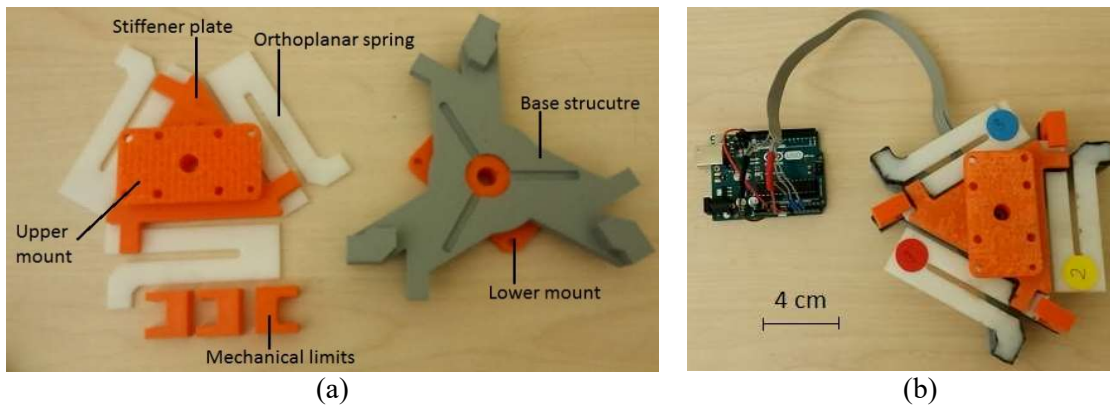


**Figure 6.10:** (a) Fabricated components and (b) completed prototype.

#### 6.4 Signal Processing

An Arduino Uno microcontroller was used to read and process the voltage signals from the prototype sensor. A cable was constructed that connects the Hall-effect sensor terminals to the input-output pins of the microcontroller. The calibration law developed in Chapter 7 was implemented on the

microcontroller as well as a feature that zeroed the sensor when it is turned on. To zero the sensor, 1000 measurements are recorded and the average measurement in each axis is found; these averages are then subtracted from all future measurements.

The analog-to-digital converter used has a 10-bit resolution and a 3.3-volt reference is used, this yields a voltage quantization error of

$$Q = \frac{3.3}{2^{10}} = 0.0032 \text{ V} \quad (6.6)$$

There are other conversion errors present in an analog-to-digital converter, including hysteresis, linearity, sensitivity, zero, and repeatability errors. The overall error of the sensor will be estimated in Chapter 7 by testing and uncertainty analysis.

## Chapter 7: Calibration and Testing

In this chapter, the calibration of the developed prototype and its testing are presented. Methods used to calibrate the sensor are discussed and various calibration laws are evaluated. An important performance parameter of a sensor is its instrument uncertainty, which is an estimate of the errors in the sensor's measurements. In robotic force control applications, instrument uncertainty of the force/torque sensor will ultimately determine how accurately the robot can sense its environment and consequently how accurately the robot may apply forces to its environment. Tests were done to determine the sensor's drift, repeatability, and noise; the results of these tests and the calibration were used to determine the instrument uncertainty of the developed force/torque sensor.

### 7.1 Sensor Calibration

#### 7.1.1 Calibration Data Acquisition

An attachment for the sensor was laser cut so that weights could be applied to the sensor and generate moments as well as forces. The attachment consists of lever arms along the x and z axes of the sensor frame, as shown in Figure 7.1. Markings were made on the attachment to apply weights at specified locations to generate various known moments. The sensor was mounted on a tripod with the attachment in place for calibration data acquisition.

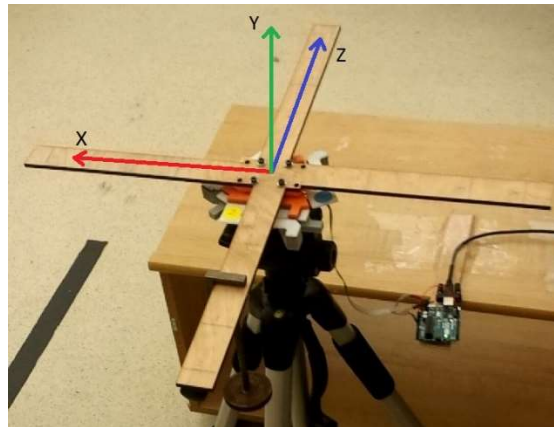


**Figure 7.1:** Attachment for applying forces and moments using weights.

An Arduino Uno microcontroller was used to read voltages from the Hall-effect sensors. To minimize the effect of noise in the voltage readings during the calibration, each calibration data point is based on the average of 10,000 individual voltage readings. Precautions were also taken to avoid the effects of creep of the orthoplanar spring during the calibration- between each loading, each average voltage output of the sensor was allowed to recover to within 0.005 volts of its original value before the next weight was applied. Furthermore, the direction of the applied moment was alternated between the acquisition of consecutive data points to reduce the effect of creep.

A calibration is performed by applying a range of forces and moments to the sensor and recording the voltage output. The calibration test plan was designed to consider each combination of force and moment components. To this end,  $F_y - M_x$ ,  $F_y - M_z$ , and  $M_x - M_z$  calibration data was gathered yielding a total of 87 data points. A three-dimensional plot of the applied force and moment data points ( $M_x, M_z, F_y$ ) is shown in Figure 7.2. The data covers a range of forces and moments given in Table 7.1. Here a negative force is one that compresses the sensor. Only negative forces were applied due to limitations in the calibration equipment, however, for the calibration laws based on physical reasoning discussed in section 7.1.3 extrapolation to positive forces should be acceptable. Furthermore, measurement of negative forces only is sufficient for many contact tasks.

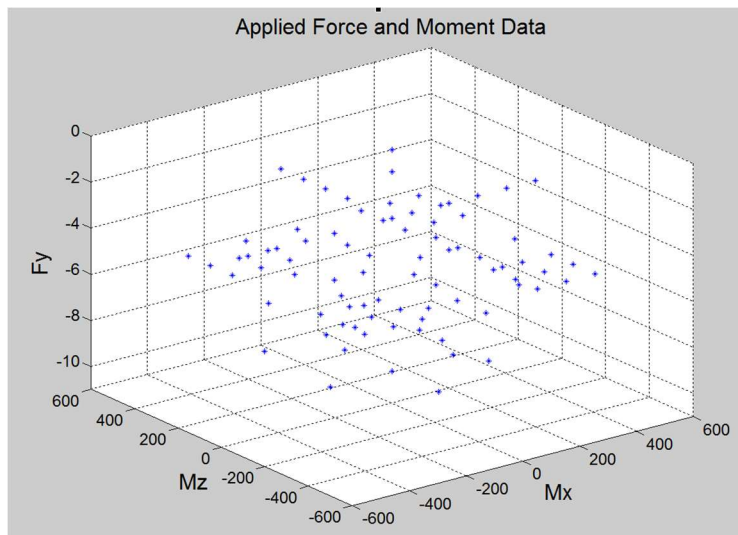


**Figure 7.2:** Three dimensional plot of applied force and moment calibration data, ( $M_x, M_z, F_y$ ).

**Table 7.1:** Maximum and minimum values of applied forces and moments during calibration.

	$F_y$ (N)	$M_x$ (N · mm)	$M_z$ (N · mm)
<b>Maximum</b>	0	507.15	507.15
<b>Minimum</b>	-9.614	-507.15	-507.15

### 7.1.2 Linear and Quadratic Calibration Laws

Once the calibration data was gathered, it was used to determine the relationship between the three Hall-effect voltages and the applied force and moment. Linear and quadratic calibration laws will be discussed in this section. The linear curve fit has a general form given by

$$F_{yFit} = a_{Fy1}v_1 + a_{Fy2}v_2 + a_{Fy3}v_3 \quad (7.1)$$

$$M_{xFit} = a_{Mx1}v_1 + a_{Mx2}v_2 + a_{Mx3}v_3 \quad (7.2)$$

$$M_{zFit} = a_{Mz1}v_1 + a_{Mz2}v_2 + a_{Mz3}v_3 \quad (7.3)$$

where  $v_i$  is the change in voltage output of the  $i$ th Hall-effect sensor caused by the applied loads. The general form of the quadratic curve fit is given by

$$F_{yFit} = a_{Fy1}v_1 + a_{Fy2}v_2 + a_{Fy3}v_3 + a_{Fy4}v_1^2 + a_{Fy5}v_2^2 + a_{Fy6}v_3^2 + a_{Fy7}v_1v_2 + a_{Fy8}v_1v_3 + a_{Fy9}v_2v_3 \quad (7.4)$$

$$M_{xFit} = a_{Mx1}v_1 + a_{Mx2}v_2 + a_{Mx3}v_3 + a_{Mx4}v_1^2 + a_{Mx5}v_2^2 + a_{Mx6}v_3^2 + a_{Mx7}v_1v_2 + a_{Mx8}v_1v_3 + a_{Mx9}v_2v_3 \quad (7.5)$$

$$M_{zFit} = a_{Mz1}v_1 + a_{Mz2}v_2 + a_{Mz3}v_3 + a_{Mz4}v_1^2 + a_{Mz5}v_2^2 + a_{Mz6}v_3^2 + a_{Mz7}v_1v_2 + a_{Mz8}v_1v_3 + a_{Mz9}v_2v_3 \quad (7.6)$$

In the linear and quadratic curve fits, there is no constant term; ideally this ensures that the sensor indicates zero force and moment when there is no load applied. The coefficients of each curve were then chosen to minimize the sum of the squared residuals. To determine the coefficients  $a_{Fy}$ ,  $a_{Mx}$ , and  $a_{Mz}$ , the force/torque data and voltage data were arranged into the following matrix equations:

$$\begin{bmatrix} F_{y1} \\ F_{y2} \\ \vdots \\ F_{yn} \end{bmatrix} = V \begin{bmatrix} a_{Fy1} \\ a_{Fy2} \\ \vdots \\ a_{Fym} \end{bmatrix} + \begin{bmatrix} \delta F_{y1} \\ \delta F_{y2} \\ \vdots \\ \delta F_{yn} \end{bmatrix} \quad (7.7)$$

$$\begin{bmatrix} M_{x1} \\ M_{x2} \\ \vdots \\ M_{xn} \end{bmatrix} = V \begin{bmatrix} a_{Mx1} \\ a_{Mx2} \\ \vdots \\ a_{Mxm} \end{bmatrix} + \begin{bmatrix} \delta M_{x1} \\ \delta M_{x2} \\ \vdots \\ \delta M_{xn} \end{bmatrix} \quad (7.8)$$

$$\begin{bmatrix} M_{z1} \\ M_{z2} \\ \vdots \\ M_{zn} \end{bmatrix} = V \begin{bmatrix} a_{Mz1} \\ a_{Mz2} \\ \vdots \\ a_{Mzm} \end{bmatrix} + \begin{bmatrix} \delta M_{z1} \\ \delta M_{z2} \\ \vdots \\ \delta M_{zn} \end{bmatrix} \quad (7.9)$$

where  $[F_{y1} \ F_{y2} \ \dots \ F_{yn}]^T$ ,  $[M_{x1} \ M_{x2} \ \dots \ M_{xn}]^T$ ,  $[M_{z1} \ M_{z2} \ \dots \ M_{zn}]^T$  are the vectors of  $n$  force and moment data points;  $[\delta F_{y1} \ \delta F_{y2} \ \dots \ \delta F_{yn}]^T$ ,  $[\delta M_{x1} \ \delta M_{x2} \ \dots \ \delta M_{xn}]^T$ , and  $[\delta M_{z1} \ \delta M_{z2} \ \dots \ \delta M_{zn}]^T$  are the vectors of curve fit residuals; and the matrix  $V$  is given by

$$V = \begin{bmatrix} v_{11} & v_{21} & v_{31} \\ v_{12} & v_{22} & v_{32} \\ \vdots & \vdots & \vdots \\ v_{1n} & v_{2n} & v_{3n} \end{bmatrix} \quad (7.10)$$

and

$$V = \begin{bmatrix} v_{11} & v_{21} & v_{31} & v_{11}v_{21} & v_{11}v_{31} & v_{21}v_{31} & v_{11}^2 & v_{21}^2 & v_{31}^2 \\ v_{12} & v_{22} & v_{32} & v_{12}v_{22} & v_{12}v_{32} & v_{22}v_{32} & v_{12}^2 & v_{22}^2 & v_{32}^2 \\ \vdots & \vdots & \vdots & \vdots & \vdots & \vdots & \vdots & \vdots & \vdots \\ v_{1n} & v_{2n} & v_{3n} & v_{1n}v_{2n} & v_{1n}v_{3n} & v_{2n}v_{3n} & v_{1n}^2 & v_{2n}^2 & v_{3n}^2 \end{bmatrix} \quad (7.11)$$

for the linear and quadratic cases respectively.  $v_{ij}$  is the change in voltage output from the  $i$ th Hall-effect sensor during the application of the  $j$ th loading ( $j$ th data point). The coefficients are solved for using the Moore-Penrose pseudoinverse of  $V$ , resulting in a least squares curve fit. The pseudoinverse is given by

$$V^* = (V^T V)^{-1} V^T \quad (7.12)$$

The coefficients  $a_{Fy}$ ,  $a_{Mx}$ , and  $a_{Mz}$  can then be found by

$$\begin{bmatrix} a_{Fy1} \\ a_{Fy2} \\ \vdots \\ a_{Fym} \end{bmatrix} = V^* \begin{bmatrix} F_{y1} \\ F_{y2} \\ \vdots \\ F_{yn} \end{bmatrix} \quad (7.13)$$

$$\begin{bmatrix} a_{Mx1} \\ a_{Mx2} \\ \vdots \\ a_{Mxm} \end{bmatrix} = V^* \begin{bmatrix} M_{x1} \\ M_{x2} \\ \vdots \\ M_{xn} \end{bmatrix} \quad (7.14)$$

$$\begin{bmatrix} a_{Mz1} \\ a_{Mz2} \\ \vdots \\ a_{Mzm} \end{bmatrix} = V^* \begin{bmatrix} M_{z1} \\ M_{z2} \\ \vdots \\ M_{zn} \end{bmatrix} \quad (7.15)$$

Using the above method, the curve fits for the collected calibration data were found to be

$$F_{yFit} = 10.5097v_1 + 11.0802v_2 + 10.5470v_3 \quad (7.16)$$

$$M_{xFit} = -1028.7v_1 + 509.4v_2 + 529.9v_3 \quad (7.17)$$

$$M_{zFit} = -17.7140v_1 + 894.7732v_2 - 859.7298v_3 \quad (7.18)$$

for the linear curve fit and

$$F_{yFit} = 12.1595v_1 + 12.9064v_2 + 12.0631v_3 + 5.3745v_1^2 + 5.6279v_2^2 \quad (7.19)$$

$$+ 5.0898v_3^2 - 2.2634v_1v_2 - 2.4281v_1v_3 - 2.7891v_2v_3$$

$$M_{xFit} = -1289.8v_1 + 619.2v_2 + 638.7v_3 - 688.3v_1^2 + 295.7v_2^2 + 297.4v_3^2 \quad (7.20)$$

$$- 32.2v_1v_2 - 41.2v_1v_3 + 8.2v_2v_3$$

$$M_{zFit} = -23.1v_1 + 1127.8v_2 - 1079.6v_3 - 7.5v_1^2 + 642.6v_2^2 - 584.8v_3^2 \quad (7.21)$$

$$- 16.4v_1v_2 - 3v_1v_3 - 34.2v_2v_3$$

for the quadratic curve fit. Goodness of fit criteria are evaluated in section 7.1.4.

### 7.1.3 Calibration Laws Based on Physical Reasoning

In this section, the underlying mechanics of the force/torque sensor is used to obtain a theoretical form of the calibration curve. Three methods are then used to determine the parameters of this curve; the first is based on Hall-effect sensor calibration data and force and moment data, the second uses information about the magnets and force and moment data, and the third uses force and moment calibration data only. In Chapter 5, a model of the force/torque sensor was developed; the form of the calibration law used in this section was derived directly from this model.

The force and moment acting on the sensor in the measurement axes are given by

$$\begin{bmatrix} F_y \\ M_x \\ M_z \end{bmatrix} = C^{-1}J \begin{bmatrix} y_1 - y_0 \\ y_2 - y_0 \\ y_3 - y_0 \end{bmatrix} \quad (7.22)$$

and



$$y_i = \sqrt{\left(\frac{a}{B_i}\right)^{\frac{2}{3}} - R^2} \quad (7.23)$$

where  $C^{-1}$  is the inverse of the compliance matrix given by equation 5.4,  $y_i$  is the deflection of the sensor at the  $i$ th Hall-effect sensor-magnet pair, and  $B_i$  is the magnetic field strength at the  $i$ th Hall-effect sensor.

The other variables were defined and discussed in Chapter 5. Equation 7.22 may be rewritten as

$$\begin{bmatrix} F_y \\ M_x \\ M_z \end{bmatrix} = A \begin{bmatrix} y_1 \\ y_2 \\ y_3 \end{bmatrix} + D \quad (7.24)$$

where  $A$  and  $D$  depend on  $C$ ,  $J$ , and  $y_0$ . The first and second physical reasoning based calibration law may be obtained by allowing the elements of the matrices  $A$  and  $D$  to be curve fit parameters. Voltage data is used to calculate  $y_i$  data using equation 7.23 and the relationship between magnetic field and Hall-effect sensor voltage, which is given by

$$B_i = \pm \frac{1}{K}(v_i - v_0) \quad (7.25)$$

where a plus or minus is used depending on whether the north or south pole of the magnet faces the Hall-effect sensor. The first mechanics based calibration law was found by determining  $a$  and  $R$  in equation 7.23 using Hall-effect sensor calibration data. The second mechanics based calibration law was found by determining  $a$  and  $R$  in equation 7.23 using the properties of the magnets used. In both the first and second calibration methods, the applied force and moment data is used to find the elements of  $A$  and  $D$  yielding a least squares regression. The third mechanics based calibration method does not rely on any known properties, except for the Hall-effect sensor's quiescent voltage output  $v_0$ . The rest of the parameters in the general equation derived from the sensors mechanics are considered curve fit parameters. This calibration law can be written as

$$F_y = \sum_{i=1}^3 \sqrt{\left(\frac{c_{Fy(2i-1)}}{\pm(v_i - v_0)}\right)^{\frac{2}{3}} - c_{Fy(2i)}^2} + c_{Fy7} \quad (7.26)$$

$$M_x = -\sqrt{\left(\frac{c_{Mx1}}{\pm(v_i - v_0)}\right)^{\frac{2}{3}} - c_{Mx2}^2} + \sum_{i=2}^3 \sqrt{\left(\frac{c_{Mx(2i-1)}}{\pm(v_i - v_0)}\right)^{\frac{2}{3}} - c_{Mx2i}^2} + c_{Mx7} \quad (7.27)$$

$$M_z = \sum_{i=1}^3 (-1)^i \sqrt{\left(\frac{c_{Mz(2i-1)}}{\pm(v_i - v_0)}\right)^{\frac{2}{3}} - c_{Mz(2i)}^2} + c_{Mz7} \quad (7.28)$$

where  $v_i$  is the output voltage of Hall-effect sensor  $i$  and  $c_{Fy1}, c_{Fy2}, \dots, c_{Mz7}$  are the curve fit parameters. The curve fit parameters were determined by a Matlab function called `nlinfit` which uses the Levenberg-Marquardt algorithm to find the curve fit parameters that result in a local minimum of the sum of the squared residuals.

Each of the three mechanics based calibration methods were implemented on the prototype sensor. For the first method, Hall-effect sensor  $(y, v)$  data was gathered to determine  $a$  and  $R$  based on a Hall-effect sensor calibration. A plot of the data gathered is shown in Figure 7.3a; this data was linearized based on a model of the magnetic field-distance relationship given by equation 7.23. The linearized data is shown in Figure 7.3b, where the independent variable is  $1/(v - v_0)^{\frac{2}{3}}$  as per the linearized equation. A linear least squares curve fit to the linearized data resulted in

$$y^2 = 89.783 \left( \frac{1}{(v - v_0)^{\frac{2}{3}}} \right) - 24.55 \quad (7.29)$$

where the Hall-effect sensor quiescent voltage output  $v_0$  was 2.5 volts for the prototype design. Force and moment calibration data was then used to determine  $A$  and  $D$  in equation 7.24. Using the positive square root of the right-hand-side of equation 7.29, voltages were converted into displacements  $y_i$  at each Hall-effect sensor.  $A$  and  $D$  were found to be

$$A = \begin{bmatrix} 2.8018 & 2.8711 & 2.6510 \\ -260.31 & 127.11 & 128.63 \\ -4.3314 & 221.25 & -206.09 \end{bmatrix} \quad (7.30)$$

and

$$D = \begin{bmatrix} -75.232 \\ 0.6579 \\ -78.624 \end{bmatrix} \quad (7.31)$$

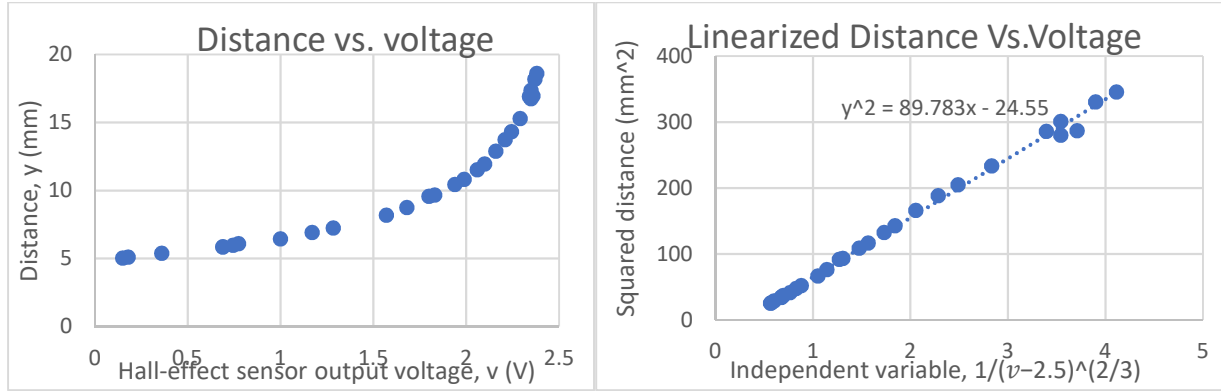


**Figure 7.3:** (a) Hall-effect sensor voltage vs. distance data and (b) linearized data.

The second calibration method uses a similar calibration law as the first method, except different values for  $a$  and  $R$  are used. Equation 5.9 is used to find  $a$  based on magnet properties and  $R$  is set equal to the radius of the magnets. Using a similar method as physical reasoning based calibration one,  $A$  and  $D$  were determined to be

$$A = \begin{bmatrix} 2.5166 & 2.5740 & 2.3723 \\ -233.85 & 113.92 & 115.09 \\ -3.9127 & 198.33 & -184.42 \end{bmatrix} \quad (7.32)$$

and

$$D = \begin{bmatrix} -88.956 \\ 16.319 \\ -99.624 \end{bmatrix} \quad (7.33)$$

Finally, the parameters of the third calibration law were evaluated using Matlab as discussed above and are shown in Table 7.2

**Table 7.2:** Curve fit parameters for physical reasoning based calibration law three.

$F_y$		$M_x$		$M_z$	
$c_{Fy1}$	712.30	$c_{Mx1}$	$6.6266 \times 10^6$	$c_{Mz1}$	$3.2436 \times 10^4$
$c_{Fy2}$	188.90	$c_{Mx2}$	$1.3596 \times 10^6$	$c_{Mz2}$	$-4.4575 \times 10^5$
$c_{Fy3}$	720.03	$c_{Mx3}$	$1.2411 \times 10^6$	$c_{Mz3}$	$7.3374 \times 10^6$
$c_{Fy4}$	212.03	$c_{Mx4}$	$4.789 \times 10^5$	$c_{Mz4}$	$-1.8686 \times 10^6$
$c_{Fy5}$	546.64	$c_{Mx5}$	$1.1849 \times 10^6$	$c_{Mz5}$	$4.1213 \times 10^6$
$c_{Fy6}$	207.75	$c_{Mx6}$	$5.1492 \times 10^5$	$c_{Mz6}$	$8.5936 \times 10^5$
$c_{Fy7}$	-71.818	$c_{Mx7}$	$5.6905 \times 10^2$	$c_{Mz7}$	$-5.2934 \times 10^2$

#### 7.1.4 Evaluation of Calibration Laws

The ability to accurately deduce the force and moment acting on the sensor based on a calibration law is limited because of curve fit residual errors and random errors in the force and moment data [41]. The residual errors are quantified by the root mean square error given by

$$\delta F_{rms} = \sqrt{\frac{\sum_{i=1}^n (F_i - F_{ci})^2}{\vartheta}} \quad (7.34)$$

where  $F_i$  is the  $i$ th force or moment data point,  $F_{ci}$  is the corresponding force or moment predicted by the calibration law, and  $\vartheta$  is the degrees of freedom of the curve fit. The degree of freedom of a curve fit is given by  $\vartheta = n - m$  where  $m$  is the number of curve fit parameters.

Random errors in the force and moment data give rise to uncertainty in the parameters of the curve fits. For the linear and quadratic calibration laws, the uncertainty in the curve fit coefficients may be found by computing the parameter covariance matrix given by [37]

$$Var_a = \delta F (V^T V)^{-1} \quad (7.35)$$

The standard error of the coefficients is given by the square root of the diagonal terms of  $Var_a$ . Error in the curve fit coefficients leads to error in the deduced force and moment which is evaluated at each data point by

$$\Delta F_{Fit} = V (Var_a) V^T \quad (7.36)$$

where  $\Delta F_{Fit}$  is an  $n$ -by- $n$  matrix whose diagonal elements are the squares of the standard errors of the fit for each data point [41]. Finally, the standard error in the force or moment prediction is the result of the combined residual errors and errors in the curve fit coefficients and can be estimated by

$$\delta F_{pred.} = \sqrt{Max(diag(\Delta F_{Fit})) + \delta F_{rms}^2} \quad (7.37)$$

The maximum diagonal element of  $\Delta F_{Fit}$  is used because it is expected to be a reasonable approximation of a 95% confidence uncertainty. The standard prediction error is evaluated similarly for the first and second physical reasoning based calibration laws, except  $V$  is replaced with  $Y$ , where  $Y$  is given by

$$Y = \begin{bmatrix} y_{11} & y_{21} & y_{31} & 1 \\ y_{12} & y_{22} & y_{32} & 1 \\ \vdots & \vdots & \vdots & \vdots \\ y_{1n} & y_{2n} & y_{3n} & 1 \end{bmatrix} \quad (7.38)$$

and  $y_{ij}$  is the  $i$ th Hall-effect sensor displacement calculated by equation 7.23 for the  $j$ th data point. The standard prediction error of the third physical reasoning based calibration law was evaluated using built-in Matlab functions.

The root mean square error and standard prediction error of each calibration law is shown in Table 7.3. It can be seen that the linear calibration law is a relatively poor fit. The quadratic calibration law drastically improves the fit compared to the linear, however, the best calibration laws were found to be physical reasoning based. There is little difference observed between the three physical reasoning based calibration laws, however, the easiest one to implement was the second. This is because method one requires the extra step of calibrating the Hall-effect sensors, while method three relies on guessing a set of initial parameters for the iterative least squares estimation algorithm. It is very difficult to find an absolute minimum; therefore, different initial guesses yield different curve fit parameters which may not correspond to an absolute minimum. Physical reasoning based calibration law two was chosen for implementation of the sensor for robotic force control, which is discussed in Chapter 9 and was used in the tests discussed in the rest of this chapter.

**Table 7.3:** Calibration root mean square errors and standard prediction errors.

Calibration	RMS_Fy (N)	RMS_Mx (N-mm)	RMS_Mz (N-mm)	Upred_Fy (95%) (N)	Upred_Mx (95%) (N-mm)	Upred_Mz (95%) (N-mm)
Linear	0.3934	26.82	31.97	0.9720	66.37	79.11
Quadratic	0.0958	9.600	7.039	0.2673	26.79	19.64
Physical reasoning based 1	0.0773	7.322	6.104	0.1915	18.13	15.11
Physical reasoning based 2	0.0839	7.534	5.600	0.2076	18.65	13.86
Physical reasoning based 3	0.0773	7.327	5.414	0.2048	19.37	14.08

## 7.2 Instrument Uncertainty

Any measurement system will have elemental errors which cause the measurements produced by the system to contain error; the possible range of this error is estimated by uncertainty [36]. Tests may be done to determine estimates of each type of error inherent in the measurement system, then each of the error estimates may be combined into an overall estimate of the instrument error which is called the instrument uncertainty. This approach was used in [37], where uncertainty was determined by the combined effects of calibration errors, sensor drift, and sensor noise. In this thesis, four elemental errors were considered in determining the instrument uncertainty of the developed force/torque sensor: calibration error, sensor drift, sensor repeatability, and sensor noise. The calibration error is determined from the analysis in section 7.1.4. Tests were performed on the prototype to estimate the other elemental errors.

### 7.2.1 Sensor Drift

Drift occurs when the sensor indicates a change in force or moment under a constant load and is thought to be caused by the viscoelasticity of the orthoplanar spring material. Drift shows up as an error in the sensors measurements and therefore is an important contribution to the instrument uncertainty. To determine the contribution of drift to the instrument uncertainty, ten drift tests were performed using a setup similar to that used for calibration. In each drift test, a constant load was applied to the sensor and the sensor's output was recorded over time. The uncertainty due to drift was quantified by the change in force or moment indicated by the sensor while under a constant load over the course of ten minutes. The drift error can be expressed as a percent error given by

$$Error_{drift} = 100 \times \frac{F_f - F_0}{F_0} \quad (7.39)$$

where  $F_0$  and  $F_f$  are the force or moment readings before and after drift has occurred respectively.

Determining  $F_0$  is complicated because there is no clear initial force or moment reading- the force and moment readings continuously rise from a zero value as the force or moment is applied. To overcome this complication, the initial reading for each drift test was calculated by an algorithm which is shown in Figure 7.4. Determining the final force or moment reading is more straightforward; force or moment

readings were taken for 10.3 minutes for each test; the readings were averaged from 9.7 to 10.3 minutes to yield a standardized final reading at 10 minutes while minimizing the effect of sensor noise. The results of each drift test are shown in Table 7.4. The percent errors due to drift can be seen to vary from approximately 5% to 10%, therefore, a 95% confidence uncertainty will be estimated to be 10% of the sensor output. The uncertainty contribution of drift is therefore given by

$$U_{drift} = 0.1F \quad (7.40)$$

where  $F$  is either a force or moment measured by the sensor.

**Table 7.4:** Results of drift tests.

Test	Initial Force (N) or Moment (N-mm)	Final Force (N) or Moment (N-mm)	Relative Error %
1	$F_y = -5.04$	$F_y = -5.28$	4.7
2	$F_y = -9.35$	$F_y = -10.2$	9.0
3	$M_z = -205.2$	$M_z = -223.6$	9.0
4	$M_z = -514.2$	$M_z = -563.4$	9.6
5	$M_x = 205.1$	$M_x = 225.1$	9.7
6	$M_x = -219.1$	$M_x = -228.2$	4.1
7	$M_z = 203.8$	$M_z = 222.3$	9.1
8	$M_x = 519$	$M_x = 572.4$	10
9	$M_x = -514.6$	$M_x = -556.2$	8.1
10	$M_z = 508.5$	$M_z = 554.6$	9.1

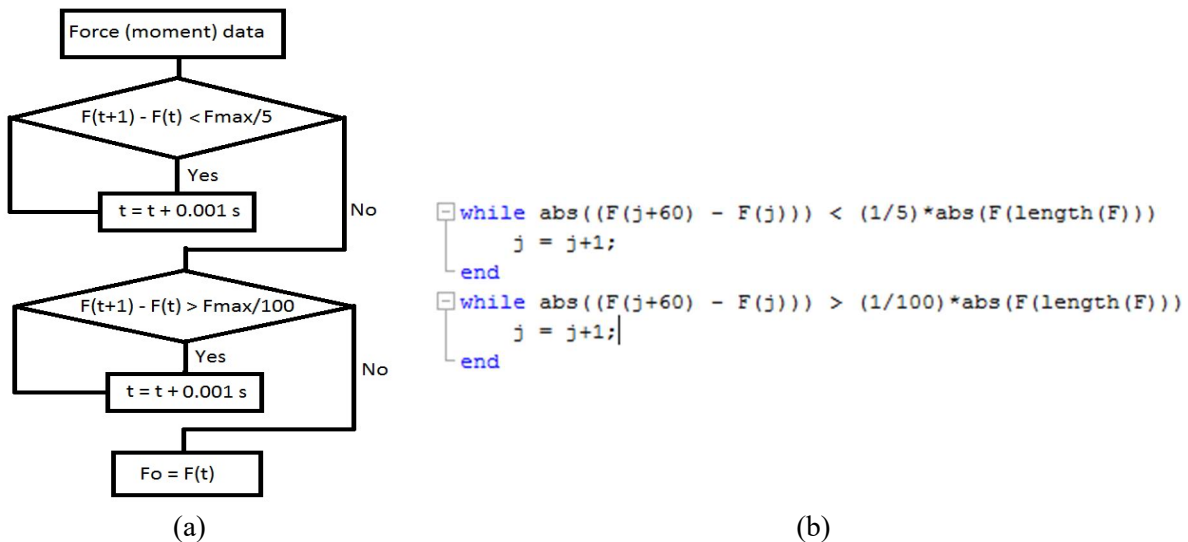


**Figure 7.4:** Algorithm for determining initial force value at the start of the drift tests; (a) algorithm flow chart and (b) Matlab code implementing algorithm.

## 7.2.2 Instrument Repeatability

Instrument repeatability is a measure of an instruments ability to indicate consistent measurements under the independent application of identical inputs [36]. To determine the instrument repeatability of the sensor, a variety of loadings were applied to obtain a set of sensor readings using the same setup used in the calibration test. The same set of loads were repeatedly applied to the sensor five times. To remove the effect of noise during the repeatability tests, each recorded reading was the average of a 10,000 recorded values of the sensor output at a constant applied load. For a given loading, the sensor readings varied with standard deviations as shown in Table 7.5. The maximum standard deviations for each measurement axis were used to estimate the uncertainty due to repeatability at a 95% confidence interval. The resulting uncertainty in each axis at a 95% confidence interval is shown in Table 7.6.

**Table 7.5:** Standard deviations of repeatability test data.

Nominal Applied Load			Std. Dev. of Sensor Force (Moment) Readings		
$F_y (N)$	$M_x (N \cdot mm)$	$M_z (N \cdot mm)$	$F_y (N)$	$M_x (N \cdot mm)$	$M_z (N \cdot mm)$
-0.95	0	0	0.0507	0.3372	0.5103
-2.98	0	-203	0.0459	0.8467	1.116
-2.98	0	203	0.0572	0.2686	1.599
-2.98	0	-507	0.0361	0.6454	1.807
-2.98	0	507	0.0422	0.5743	1.782
-2.98	203	0	0.0322	0.2834	0.7494
-2.98	-203	0	0.0273	0.8587	1.033
-2.98	507	0	0.0259	2.415	0.6894
-2.98	-507	0	0.0237	2.050	0.9082
-5.01	0	0	0.0256	1.514	0.9416
-9.61	0	0	0.0231	1.658	2.134

**Table 7.6:** Uncertainties due to instrument repeatability.

	$F_y (N)$	$M_x (N \cdot mm)$	$M_z (N \cdot mm)$
Uncertainty (95%)	0.147	6.210	5.486

## 7.2.3 Sensor Noise

Sensor noise results from analog-to-digital conversions, Hall-effect sensor output noise, and various other sources. To determine the amount of noise present, sensor readings were recorder at no load and the standard deviation of 83 force and moment readings was calculated. Uncertainty at the 95% confidence level was then calculate by multiplying the standard deviation by a coverage factor of two. The



results are given in Table 7.7. Noise may be reduced by using a higher resolution analog-to-digital converter and a low-pass filter.

**Table 7.7:** Standard deviation and uncertainty at 95% confidence of sensor noise.

	$F_y$ (N)	$M_x$ (N · mm)	$M_z$ (N · mm)
<b>Noise Std. Dev.</b>	0.0654	3.992	3.986
<b>Uncertainty (95%)</b>	0.1308	7.985	7.973

### 7.2.4 Overall Instrument Uncertainty

The overall instrument uncertainty may now be determined by combining the contributions due to calibration errors, drift, repeatability, and noise by the root sum square (RSS) method. The overall instrument uncertainty is thus given by

$$U_c = \sqrt{U_{calib}^2 + U_{drift}^2 + U_{Rep}^2 + U_{Noise}^2} \quad (7.41)$$

where  $U_{calib}$ ,  $U_{drif}$ ,  $U_{Rep}$ , and  $U_{Noise}$  are the uncertainties due to calibration errors, drift, instrument repeatability, and noise respectively. The uncertainty in each measurement axis is computed using equation 7.41. The total uncertainty in each measurement axis is shown in shown in Table 7.8 with and without drift error included. The instrument uncertainty without drift corresponds to cases where there is a small load or the measurement time is small.

**Table 7.8:** Instrument uncertainty with and without drift error included.

<b>Measurement Axis</b>	<b><math>U_c</math> without drift</b>	<b><math>U_c</math> drift at maximum load</b>
$F_y$	0.286 (N)	1.04 (N)
$M_x$	21.2 (N-mm)	54.3 (N-mm)
$M_x$	16.9 (N-mm)	52.8 (N-mm)

### 7.3 Discussion of Results

The developed sensor's accuracy is adequate for many applications such as assistive and domestic service where very precise control of forces is not necessary. To the best of my knowledge, the instrument uncertainty of previously developed compliant force sensors has not been established in the literature, however, it is likely that the sensor developed in this thesis has at most a similar level of error. The sensor developed in [18] was reported to have a hysteresis error of 0.6 mm in translation and 0.0099 radians in rotation; a force measurement, obtained by multiplying by the appropriate stiffness of the wrist, yields force

and moment measurement errors of 4.7 N and 69 N-mm. This error is substantially larger than the uncertainty results in section 7.2, albeit the measurement range of this sensor is not known.

The accuracy of the prototype may be improved with the use of a metallic orthoplanar spring, however, design may be complicated by the lower strength-to-modulus ratio and the added damping required. Furthermore, sensor costs would be increased. A potential alternative method of reducing drift error is to model the viscoelastic creep of the sensor and correct for it using a compensation law as was done in [42], this would require extending the proposed compensation law to the case of a multi-axis sensor. It is common to use a redundant number of transducers to improve the accuracy of a measurement, therefore the uncertainty in the developed sensor is likely to improve by using redundant Hall-effect sensors.

## Chapter 8: Force Control Testing

The developed force/torque sensor was implemented on the USF Wheelchair Mounted Robotic Arm (WMRA) to validate its design for robot force control. Force control tests were done in force and moment measurement axes of the sensor. In this chapter, the WMRA robot kinematics and control are presented, followed by a description of the hardware used for force control. Next, the force control algorithm and experimental setup is described and discussed. Finally, the force control tests and their results are presented and discussed.

### 8.1 Robot Kinematics and Motion Control

Force control tests were implemented using an inner position loop based force controller where force feedback from the force sensor was used to modify velocity commands. To that end, the kinematics of the robot were required for motion control.

#### 8.1.1 Robotic Arm Kinematics

A robotic arm's kinematics is given by its Denavit-Hartenberg (D-H) parameters, which describe the robot's link and joint parameters and variables. There are four D-H parameters-  $a_i$  (link length),  $\alpha_i$  (link twist),  $d_i$  (link offset), and  $\theta_i$  (joint angle) as shown in Figure 8.1. The D-H parameters are most easily defined once the convention of link frame attachment is introduced.

Coordinate frames are attached to each link in order to specify the position and orientation of each link. The convention presented in Craig [43] is used in this thesis- this convention assigns link frames according to the following rules:

1. Frame  $i$  is attached to link  $i$ .
2. The Z-axis of frame  $i$  is along joint-axis  $i$ .
3. The X-axis of frame  $i$  is along the common normal between axis  $i$  and axis  $i + 1$ .
4. The Y-axis is defined to complete a right-handed coordinate frame

The ground frame may be chosen arbitrarily and the X-axis of the frame attached to the last link of the robot may be chosen in an arbitrary direction perpendicular to  $Z_n$  and anywhere along  $Z_n$ . Using this frame assignment convention, the D-H parameters are defined as follows [43]:

$a_i$  = the distance between  $Z_i$  and  $Z_{i+1}$  measured along  $X_i$

$\alpha_i$  = the angle between  $Z_i$  and  $Z_{i+1}$  measure about  $X_i$

$d_i$  = the distance between  $X_{i-1}$  and  $X_i$  measure along  $Z_i$

$\theta_i$  = the angle between  $X_{i-1}$  and  $X_i$  measured about  $Z_i$

The D-H parameters for the WMRA are given in Table 8.1.

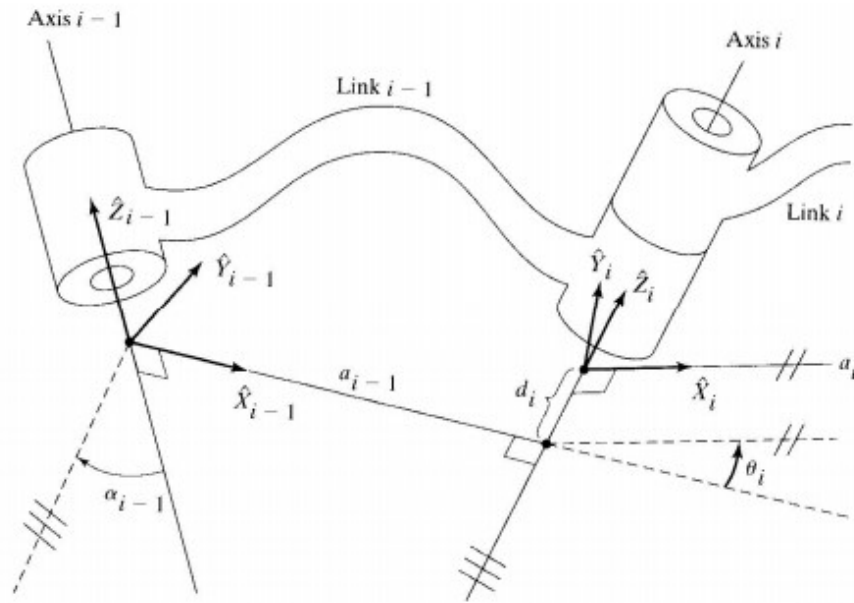


**Figure 8.1:** Link parameters, joint variables, and link frames.

**Table 8.1:** D-H parameters of WMRA.

Link/Joint	$a_{i-1}$ (mm)	$\alpha_{i-1}$ (rad)	$d_i$ (mm)	$\theta_i$
1	0	$-\pi/2$	103	$\theta_1$
2	0	$\pi/2$	133	$\theta_2$
3	0	$-\pi/2$	502	$\theta_3$
4	0	$\pi/2$	90	$\theta_4$
5	0	$-\pi/2$	375	$\theta_5$
6	0	$\pi/2$	0	$\theta_6$
7	0	$-\pi/2$	161	$\theta_7$

The forward kinematics of a robot may be determined using a robots D-H parameters and the link-frame assignment convention. The relative position and orientation of frame  $i$  with respect to frame  $i - 1$  may be expressed as a homogeneous transformation matrix given by

$${}^{i-1}T_i = \begin{bmatrix} {}^{i-1}X_i & {}^{i-1}Y_i & {}^{i-1}Z_i & {}^{i-1}P_i \\ 0 & 0 & 0 & 1 \end{bmatrix} \quad (8.1)$$

A homogeneous transformation matrix consist of four vectors- three of them are unit vectors making up the rotation matrix between the frames, and the fourth is the relative position vector between the frames. In terms of D-H parameters, the transformation matrix between adjacent link frames is given by

$${}^{i-1}T_i = \begin{bmatrix} \cos\theta_i & -\sin\theta_i & 0 & a_{i-1} \\ \sin\theta_i \cos\alpha_{i-1} & \cos\theta_i \cos\alpha_{i-1} & -\sin\alpha_{i-1} & -\sin\alpha_{i-1}d_i \\ \sin\theta_i \sin\alpha_{i-1} & \cos\theta_i \sin\alpha_{i-1} & \cos\alpha_{i-1} & \cos\alpha_{i-1}d_i \\ 0 & 0 & 0 & 1 \end{bmatrix} \quad (8.2)$$

This transformation matrix may be used to find the position and orientation of each link frame, given by

$${}^0T_j = {}^0T_1 T_2 \dots T_{j-1} T_j \quad (8.3)$$

The computation of each of the link frames was used in a method to compute the Jacobian matrix of the robot introduced in section 8.1.2. Using the equation 8.3 each link frame's position and unit vectors may be expressed as

$${}^0T_j = \begin{bmatrix} {}^0X_j & {}^0Y_j & {}^0Z_j & {}^0P_j \\ 0 & 0 & 0 & 1 \end{bmatrix} \quad (8.4)$$

### 8.1.2 Kinematics Control

The USF WMRA is a seven degree-of-freedom arm, therefore redundancy resolution is required for the inverse kinematics computation, which is in turn required to provide the robot with joint velocity commands. The relationship between joint and end-effector Cartesian velocities is given by

$$V = J\dot{\theta} \quad (8.5)$$

where  $V$  is the Cartesian velocity of the end-effector,  $J$  is a Jacobian matrix, and  $\dot{\theta}$  is the vector of joint velocities. Several methods exist to compute the Jacobian matrix- the method used in this work is based on method III presented in [44]. The Jacobian matrix based on this method is given by

$$J = \begin{bmatrix} {}^0Z_1 \times P_{17} & {}^0Z_2 \times P_{27} & {}^0Z_3 \times P_{37} & {}^0Z_4 \times P_{47} & {}^0Z_5 \times P_{57} & {}^0Z_6 \times P_{67} & {}^0Z_7 \times P_{77} \\ {}^0Z_1 & {}^0Z_2 & {}^0Z_3 & {}^0Z_4 & {}^0Z_5 & {}^0Z_6 & {}^0Z_7 \end{bmatrix} \quad (8.6)$$

where  ${}^0Z_j$  is the unit vector along the  $ith$  joint axis and  $P_{ij}$  is the relative position vector between the  $ith$  axis and the origin of the frame attached to link 7,  $P_{ij}$  given by

$$P_{j7} = {}^0P_7 - {}^0P_j \quad (8.7)$$

Redundancy resolution was accomplished by minimizing the norm of  $\dot{\theta}$  using

$$\dot{\theta} = J^*V \quad (8.8)$$

where  $J^*$  is the Moore-Penrose pseudoinverse of  $J$ , given by

$$J^* = J^T (JJ^T)^{-1} \quad (8.9)$$

The setup of the experiment ensured singularities and joint limits were avoided.

## 8.2 Force Control Implementation

### 8.2.1 Hardware

A schematic overview of the hardware used is shown in Figure 8.2. The developed force/torque sensor was installed on the wrist of the WMRA and outputs voltages to the Arduino UNO microcontroller. The microcontroller implements the calibration law discussed in Chapter 7 and outputs force and moment data in the sensor's measurement axes. The microcontroller is connected to a computer through a USB port. The computer, which interfaces with the robot's motor controllers, runs a program that computes joint velocity commands using the force feedback from the microcontroller and a force control law.

### 8.2.2 Control Algorithm

The control algorithm was implemented in Microsoft Visual Studio. A flowchart of the algorithm is shown in Figure 8.3. The inputs to the program are the robots D-H parameters and initial joint angles as well as desired contact force. The data from the developed force/torque sensor's microcontroller is parsed to obtain the desired force and moment measurements which are used to compute the velocity commands. Forward kinematic computations are performed using the equations in section 8.1.1, followed by the calculation of the Jacobian matrix. The pseudoinverse of the Jacobian matrix is then computed to calculate the joint velocity commands using equation 8.8. The joint positions are then updated by numerically

integrating the joint velocity commands. Finally, the control algorithm reiterates starting with reading force sensor data. The program ran at an update rate of 20 – 25 Hz.

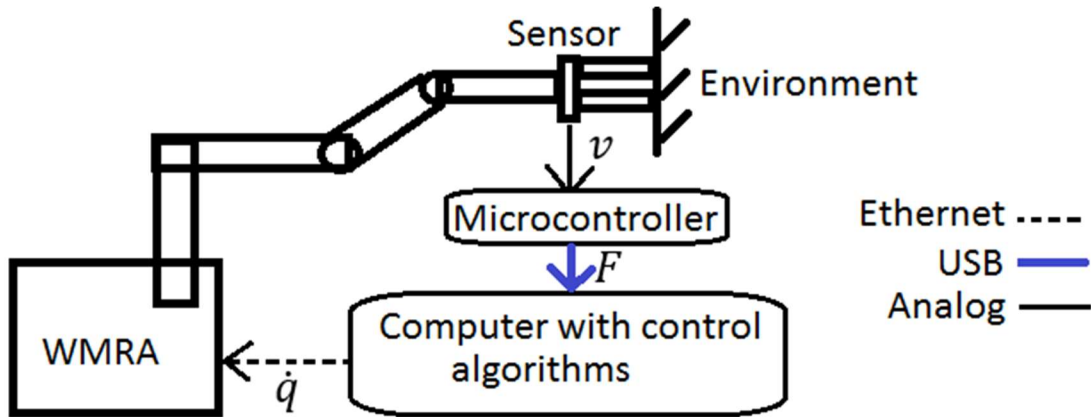


Figure 8.2: Overview of hardware used to implement force control.

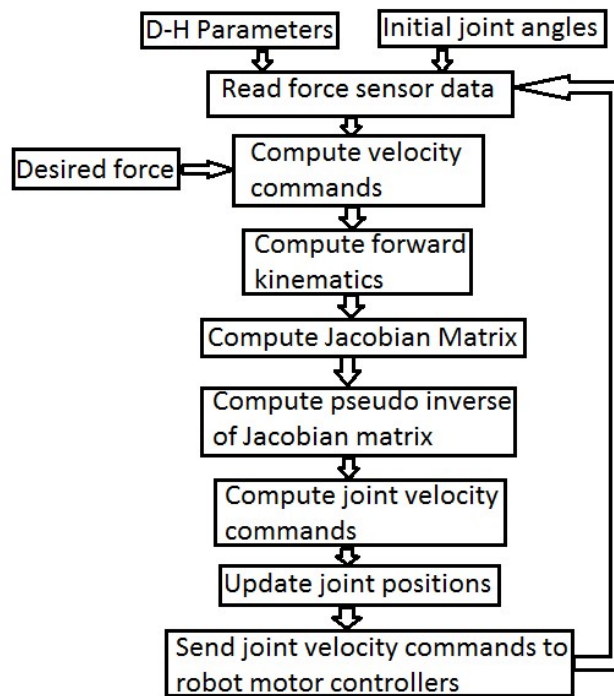


Figure 8.3: Force control algorithm flowchart.

### 8.3 Force Control Test Setup

#### 8.3.1 Task Description

Two different task setups were used to test the force and moment measurement axis of the sensor in force control, these will be referred to as setup one and two. In setup one, shown in Figure 8.4a, the robot

approaches and applies a normal force to the vertically oriented surface of the scale. In setup two, as shown in Figure 8.4b, the robot tightly grasps a vertical piece of wood and approaches and applies a force to the horizontally oriented surface of the scale. In setup two, the contact force acts at a moment arm of 22.5 cm from the sensor and thus generated a moment which is measured by one of the sensor's moment axes.



**Figure 8.4:** (a) test setup 1 using force measurement axis and (b) test setup 2 using moment axis of sensor.

### 8.3.2 Force Control Law

The force control laws used in setup one and two are given by

$$V_z = K_f (F_d - F_{sensor}) \quad (8.10)$$

and

$$V_x = K_f \left( F_d - \frac{M_{sensor}}{225} \right) \quad (8.11)$$

respectively, where  $V_z$  and  $V_x$  are the commanded velocities normal to the surface in the respective setup;  $K_f$  is the force gain, which may be different for setup one and setup two;  $F_d$  is the desired contact force; and  $F_{sensor}$  is the force measured by the sensor. The other robot end-effector velocities were commanded to be zero. Note that  $M_{sensor}$  is divided by 225 mm in the force control law of setup two in order to convert it into a measurement of the contact force acting at the 225 mm moment arm.



### 8.3.3 Force Gain Selection

The  $K_f$  values used in subsequent tests discussed in section 8.4 were selected through testing. In these tests, the sensor force or moment measurements were recorded and plotted against time as shown in Figure 8.5. For setup one, the force gain  $K_f$  was increased until there was significant overshoot; a final value of  $K_f = 5 \text{ mm}/(\text{s} \cdot \text{N})$  was chosen for test setup 1. Setup two did not experience any overshoot for the gains applied, however a quicker response was found with larger gains, therefore the largest gain tested was selected with a value of  $K_f = 13 \text{ mm}/(\text{s} \cdot \text{N})$ .

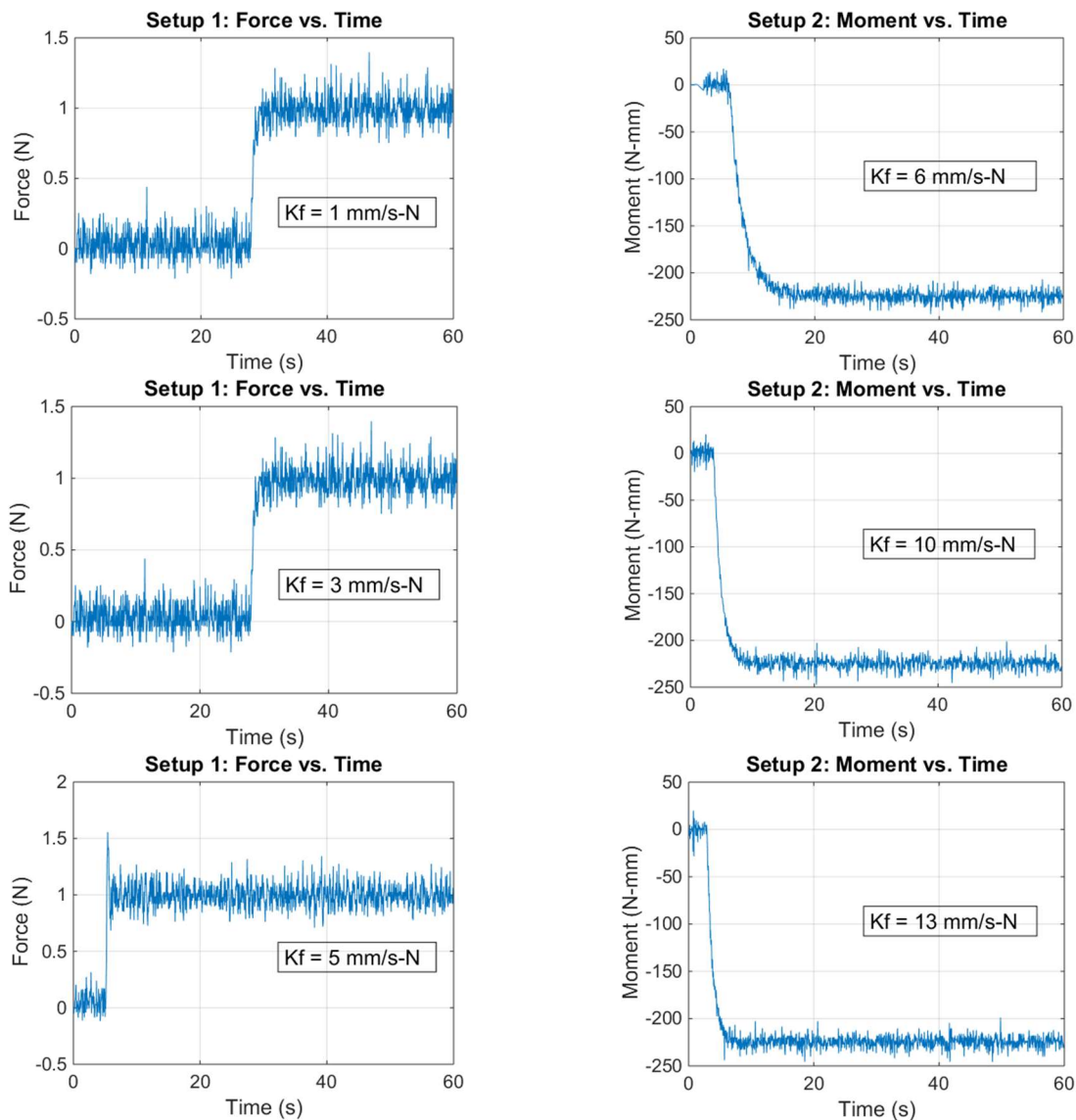


Figure 8.5: Force and moment plotted against time for varying gains.

## 8.4 Comparison to Scale Tests

Tests were performed to establish that the sensor may be successfully integrated with a robotic system and to set a benchmark for the performance obtainable with the sensor. In these tests, force measurements from an external scale were compared to the desired contact force, as well as the force indicated by the developed force/torque sensor. The contact force measurements from the scale were captured by video of the scale's output reading and the sensor data was recorded. First, tests were done using a constant desired contact force of 1 N; further tests were done with a linearly increasing desired contact force. The sensor was zeroed before each test by the method discussed in section 6.3.

### 8.4.1 Results and Discussion

The sensor and scale force and moment measurements for setup one and two are plotted against time in Figure 8.6 for the case with a constant desired contact force. The sensor readings in both setups hover around the desired values, which were 1 N for the force readings in setup one and -225 N-mm for the moment readings in setup two. The average and standard deviation of the sensor readings for both setups were found using data from 15 to 60 seconds, data from 0 to 15 seconds was left out in order to eliminate the transient phase. The moment readings from the sensor are converted into contact force by dividing by a moment arm of 225 N-mm and the corresponding contact force average and standard deviation were also found. The average and standard deviation results are shown in Table 8.2. The results show that the controller was able to drive the sensor readings to the desired value with less than a 0.5% steady-state error. The standard deviation in the sensor readings are larger than the standard deviation of the sensor's noise, which was found in Chapter 7 to be 0.0654 N and 3.992 N-mm for the force and moment axis respectively. This difference is most likely attributed to installation effects and control error.

**Table 8.2:** Force/torque sensor readings average and standard deviation.

	Setup 1 (N)	Setup 2 (N-mm)	Setup 2 (N)
<b>Average</b>	0.9951	224.7	0.9987
<b>Standard Deviation</b>	0.0941	5.528	0.0246

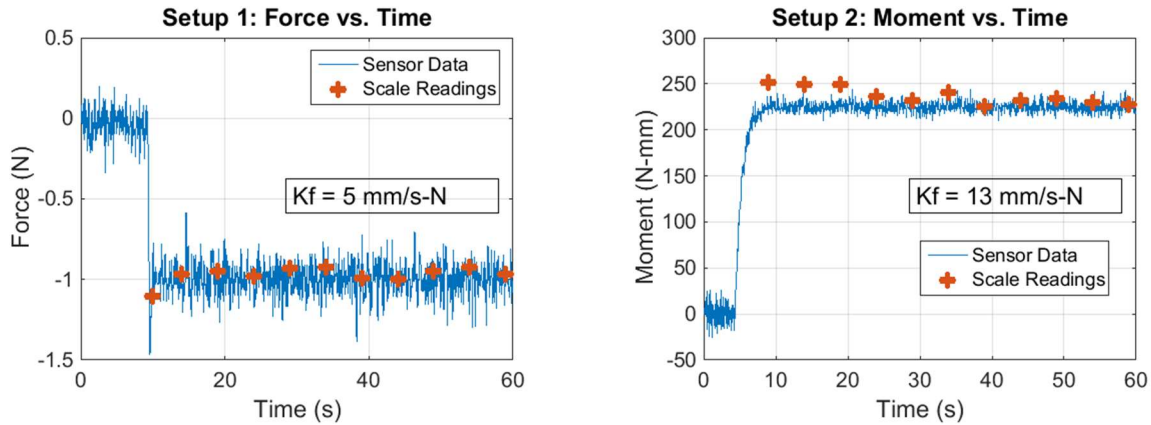


**Figure 8.6:** Force and moment plotted against time for setup one and two respectively.

The maximum and minimum contact force measurements indicated by the scale are given in Table 8.3. For setup two, the scale measurements were converted into moment measurements. The scale measurements are consistent with the desired contact force with a maximum error of 0.10 N and 0.11 N in setups one and two respectively. For setup two, the force error was converted into a moment error at the sensor by multiplying by a moment arm of 225 N-mm, the resulting moment error is 24.8 N-mm. The uncertainty analysis in Chapter 7 was found to provide a reasonable estimate of the error, where the force uncertainty was found to be 0.286 and the moment uncertainty was found to be 21.2 N-mm.

**Table 8.3:** Maximum and minimum force and moment indicated by the scale during steady-state.

	Setup 1 (N)	Setup 2 (N-mm)
<b>Maximum Reading</b>	1.01	250
<b>Minimum Reading</b>	0.90	225

The second type of testing involved applying a linearly increasing desired contact force. The force gains were reduced to 2 and 10 for setup one and two respectively to ensure stability at higher contact forces. Sensor and scale data, as well as the desired force or moment are plotted against time in Figure 8.7 for these tests. The maximum difference between the scale and sensor measurements for both setups is shown in Table 8.4. Good agreement is found between the sensor and scale measurements in setup one, however, a relatively large difference occurs in setup two at large contact forces. Further examination revealed the contact point shifts outward as the contact force increases to its maximum in setup two. This increased the moment arm, which reduced the contact force and therefore the moment measured by the scale, which was based on a fixed 225 mm moment arm. The contact point was estimated to shift by 1 to 2

cm based on further testing; this contact point motion corresponds to a moment error between 45 and 90 N-mm. It is likely the relatively large difference between the scale and sensor measurements in setup two is attributed to this contact point motion.

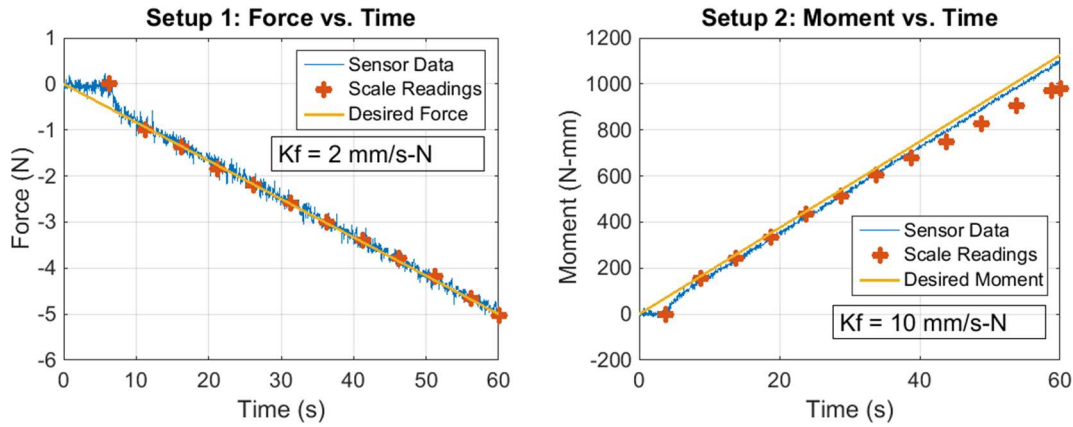


**Figure 8.7:** Sensor and scale data during testing with linearly increasing desired contact force.

**Table 8.4:** Maximum error between sensor and scale measurements with increasing desired force.

	Setup 1	Setup 2
Maximum Difference	0.217 N	114.7 N-mm

## Chapter 9: Conclusions and Future Work

### 9.1 Summary of Work

Design considerations for force/torque sensors were introduced and a novel design concept for a compliant force/torque sensor was presented. The mechanics of the design concept were discussed including methods of analyzing the sensor's compliance and stress which culminated in a mechanical design method. Models of the sensor were then developed for transducer design and calibration laws based on physical reasoning. To further study the design concept, a prototype was constructed and calibrated. A series of tests were performed on the prototype to ascertain its sensing performance, which was measured by the sensors instrument uncertainty. Finally, the sensor was implemented in robotic force control to validate its design for robot force control applications.

### 9.2 Conclusions

It was found that the analytical expressions and methods for calculating compliance and stress were in close agreement with finite element simulations. Furthermore, the calibration laws based on physical reasoning performed significantly better than linear or quadratic laws. These are indications that the analysis methods and sensor models are accurate enough for design and calibration purposes and that calibration laws based on physical reasoning should be used.

The results of prototype testing and uncertainty analysis show that a three-axis force/torque sensor may be designed using an orthoplanar spring and Hall-effect sensing. The sensor possessed reasonable measurement accuracy comparing well to previously developed compliant force/torque sensors. The results of force control testing with the sensor show that the sensor may be successfully integrated with a robotic system and allow the robot to accurately apply forces to its environment.

## 9.3 Future Work

### 9.3.1 Design Variations

Future work may involve variations in this design concept, such as the use of redundant Hall-effect sensors, different materials, and different types of compliant mechanisms. A sensor using more than three Hall-effect sensors would have several benefits. In general, the use of redundant transducers reduces measurement errors. Another benefit of redundant Hall-effect sensors is the possibility of detecting interference from external magnetic fields and perhaps correcting the output of the sensor in the presence of these fields.

The orthoplanar spring may be constructed using metals. The main benefit of a metallic orthoplanar spring is the reduced creep or stress relaxation that would be encountered, which would greatly reduce the sensor's drift error. Complications arise with metals because of their lack of damping and low strength-to-elastic modulus ratio as compared to polymers. External damping may be applied and changes in the beam geometry may be implemented to overcome these complications.

Besides or in addition to an orthoplanar spring, various compliant mechanism could be used as the elastic element of a compliant force/torque sensor. Compliant mechanisms may be developed with degrees-of-freedom in order to measure forces and moments in more than three-axes or in different axes than the currently developed sensor.

### 9.3.2 Stiffness Selection and Low Inertia End-Effector

Aside from changes in the design concept, a question remaining is what stiffness should the sensor be designed for? Stiffness selection is a tradeoff between performance in position control and force control. Through analysis and testing with sensors of varying stiffness, perhaps guidelines may be developed for the selection of sensor stiffness based on the intended applications of the robot.

The optimum stiffness of the sensor will also depend on the mass of the end-effector. If the end-effector is made lighter and the moment arm reduced, the sensor may be made more compliant thereby improving force control performance. A future project may involve the development of a lightweight

robotic gripper actuated through tendon like cables by a remote actuator. The inertia attached to the sensor may therefore be kept to a minimum.

## References

- [1] Ganwen, Z. and Hemami, A. "An Overview of Robot Force Control." *Robotica* 15.5: pp. 473-482. 1997.
- [2] Mason, Matthew T. "Compliance and Force Control for Computer Controlled Manipulators." *IEEE Transactions on Systems, Man, and Cybernetics* 11.6: pp. 418-432. 1981.
- [3] Yoshikawa, T. "Force Control of Robot Manipulators." *Proceedings. Millennium IEEE International Conference on Robotics and Automation.* 2000
- [4] Whitney, Daniel E. "Force Feedback Control of Manipulator Fine Motions." *Journal of Dynamic Systems, Measurement, and Control* 99.2: pp. 91-97. 1977.
- [5] Salisbury, J. "Active Stiffness Control of a Manipulator in Cartesian Coordinates." *19th IEEE Conference on Decision and Control including the Symposium on Adaptive Processes.* 1980.
- [6] Field, G. and Stepanenko, Y. "Model Reference Impedance Control of Robotic Manipulators." *Proceedings. IEEE Pacific Rim Conference on Communications Computers and Signal Processing:* pp. 614-617. 1993.
- [7] Raibert, M., and Craig, J. "Hybrid Position/Force Control of Manipulators." *Journal of Dynamic Systems, Measurement, and Control* 103.2: pp. 126-133. 1981
- [8] Schutter, J. D. and Van, H. "Compliant Robot Motion II. A Control Approach Based on External Control Loops." *The International Journal of Robotics Research* 7.4: pp 18-33. 1988.
- [9] Maples, J. and Becker, J. "Experiments in Force Control of Robotic Manipulators." *Proceedings. IEEE International Conference on Robotics and Automation:* pp. 695-702. 1986.
- [10] Vukobratovic, M. and Tuneski, A. "Contact Control Concepts in Manipulation Robotics-an Overview." *IEEE Transactions on Industrial Electronics* 41.1: pp. 12-24. 1994.
- [11] Roberts, R., Paul, R. and Hillberry, B. "The Effect of Wrist Force Sensor Stiffness on the Control of Robot Manipulators." *Proceedings. IEEE International Conference on Robotics and Automation:* pp. 269-274. 1985.
- [12] Eppinger, S. and Seering, W. "Three Dynamic Problems in Robot Force Control." *IEEE Transactions on Robotics and Automation* 8.6: pp. 751-758. 1992.
- [13] Chiou, B. and Shahinpoor, M. "Effect of Joint Stiffness on the Dynamic Stability of a One-link Force-controlled Manipulator." *Robotica* 7.04: pp. 398-403. 1989.
- [14] Mandal, N. and Payandeh, S. "Experimental Evaluation of the Importance of Compliance for Robotic Impact Control." *Proceedings. IEEE International Conference on Control and Applications:* pp. 511-516. 1993.



- [15] Payandeh, S. "On the Effect of Compliance in Robotic Contact Task Problem." Proceedings. American Control Conference: pp. 387-391. 1995.
- [16] Shirey, T. and Roberts, R. "Hybrid Active/passive Interaction Control for Robot Manipulators." Proceedings. Thirty-Sixth Southeastern Symposium on System Theory. pp. 441-445. 2004.
- [17] Xu, Y. and Paul, R. "A Robot Compliant Wrist System for Automated Assembly." Proceedings. IEEE International Conference on Robotics and Automation. pp. 1750-1755. 1990.
- [18] Lindsay, T., Sinha, P., and Paul, R. "An Instrumented Compliant Wrist for Robotics Applications." Proceedings. IEEE International Conference on Robotics and Automation: pp. 648-653. 1993.
- [19] Hashimoto, M. and Imamura, Y. "Design and Characteristics of a Parallel Link Compliant Wrist." Proceedings. IEEE International Conference on Robotics and Automation: pp. 2457-2462. 1994.
- [20] Schoisengeier, A., Lindenroth, L., Back, J., Qiu, C., Noh, Y., Althoefer, K., Dai, J., Rhode, K., and Liu, H. "Design of a Flexible Force-sensing Platform for Medical Ultrasound Probes." Proceedings. 6th IEEE International Conference on Biomedical Robotics and Biomechanics: pp. 278-283. 2016.
- [21] Ataollahi, A., Fallah A. S., Seneviratne, L. D., Dasgupta, P. and Althoefer, K. "Novel Force Sensing Approach Employing Prismatic-Tip Optical Fiber Inside an Orthoplanar Spring Structure." IEEE/ASME Transactions on Mechatronics 19.1: pp. 121-130. 2014.
- [22] Bekhti, R., Duchaine, V., and Cardou, P. "Miniature Capacitive Three-axis Force Sensor." Proceedings. IEEE/RSJ International Conference on Intelligent Robots and Systems: pp. 3939-3946. 2014.
- [23] Kyberd, P. J. and Chappell, P. H. "A Force Sensor for Automatic Manipulation Based on the Hall-effect." Measurement Science and Technology 4.3: pp. 281-287. 1993.
- [24] Lange, F., Jehle, C. Suppa, S., and Hirzinger, G. "Revised Force Control Using a Compliant Sensor with a Position Controlled Robot." Proceedings. IEEE International Conference on Robotics and Automation: pp. 1532-1537. 2012.
- [25] Kesner, S. B. and Howe, R. D. "Design Principles for Rapid Prototyping Forces Sensors Using 3-D Printing." IEEE/ASME Transactions on Mechatronics 16.5: pp. 866-870. 2011.
- [26] Marrone, F. and Strobel, H. "CleaningAssistant-a Service Robot Designed for Cleaning Tasks." Proceedings. IEEE/ASME International Conference on Advanced Intelligent Mechatronics: pp. 1041-1046. 2001.
- [27] Lorenz, W. A., Peshkin, M. A., and Colgate, J. E. "New Sensors for New Applications: Force Sensors for Human/robot Interaction." Proceedings. IEEE International Conference on Robotics and Automation. 1999.
- [28] Howell, L. L. Compliant Mechanisms. New York: Wiley, 2001. Print.
- [29] Su, H. J., Shi, H. and Yu, J. "A Symbolic Formulation for Analytical Compliance Analysis and Synthesis of Flexure Mechanisms." Journal of Mechanical Design 134.5. 2012.

- [30] Dai, S. and Ding, X. "Compliance Analysis of a Three-Legged Rigidly-Connected Platform Device." *Journal of Mechanical Design* 128.4. pp. 755-764. 2006.
- [31] Qiu, C., Qi, P., Liu, H., Althoefer, K. and Dai, J. S. "Six-Dimensional Compliance Analysis and Validation of Orthoplanar Springs." *Journal of Mechanical Design* 138.4. 2016.
- [32] Serway, R. and Jewett, W. "Chapter 29." *Physics for Scientists and Engineers*, 8th Edition. Brooks Cole. 2009.
- [33] McCall, W. D. and Rohan, E. J. "A Linear Position Transducer Using a Magnet and Hall-effect Devices." *IEEE Transactions on Instrumentation and Measurement* 26.2: pp. 133-36. 1977.
- [34] Kyberd, P. J. and Chappell, P. H. "A Force Sensor for Automatic Manipulation Based on the Hall-effect." *Measurement Science and Technology* 4.3: pp. 281-287. 1993.
- [35] Gorinevsky, D. M., Formalsky, A. M., Scheider, A. YU. "Chapter 3." *Force Control of Robotic Systems*.
- [36] Figliola, R. S. "Chapter 1." *Theory and Design for Mechanical Measurements*, 5th Edition. Moorpark, CA: Content Technologies. 2012.
- [37] Muntwyler, S., Beyeler, F., and Nelson, B. "Three-axis Micro-force Sensor with Sub-micro-Newton Measurement Uncertainty and Tunable Force Range." *Journal of Micromechanics and Microengineering* 20.2. 2009.
- [38] Parise, J. J., Howell, L. L., and Magleby, S. P. "Ortho-planar Linear-motion Springs." *Mechanism and Machine Theory* 36.11-12: pp. 1281-1299. 2001.
- [39] "Design Guide – Module III." Dupont Engineering Polymers: pp. 6.
- [40] <https://www.kjmagnetics.com/specs.asp> "K&J Magnetics - Specifications." Web. 05 Feb. 2017.
- [41] Gavin, H. P. *Generalized Linear Least Squares: Fitting Curves to Data and Error Analysis*. course notes for System Identification at Duke University. Fall, 2013
- [42] Kumar, N., Piccin, O., Meylheuc, L., Barbe, L., and Bayle, B. "Design and Modeling of a Polymer Force Sensor." *IEEE/ASME Transactions on Mechatronics*. 21.1: 2016.
- [43] Craig, J. J. "Chapter 3." *Introduction to Robotics: Mechanics and Control*. Upper Saddle River, NJ: Pearson/Prentice Hall, 2005.
- [44] Orin, D. E., and Schrader, W. W. "Efficient Computation of the Jacobian for Robot Manipulators." *The International Journal of Robotics Research* 3.4: pp. 66-75. 1984.
- [45] Camacho, J. M., Sosa, V. "Alternative Method to Calculate the Magnetic Field of Permanent Magnets with Azimuthal Symmetry." *Mexican Journal of Physics* 59: pp. 8-17. 2013.

## Appendix A: Effective Beam Length Data

As described in section 4.1.1, data was gathered to determine the relationship between change in effective beam length and design parameters of the orthoplanar spring's beam segments. The design parameters were defined in Figure A.1 which is repeated here. The  $(\frac{\delta L_{eff}}{c}, \frac{b}{c}, \frac{b}{h})$  data is shown in Table A.1.

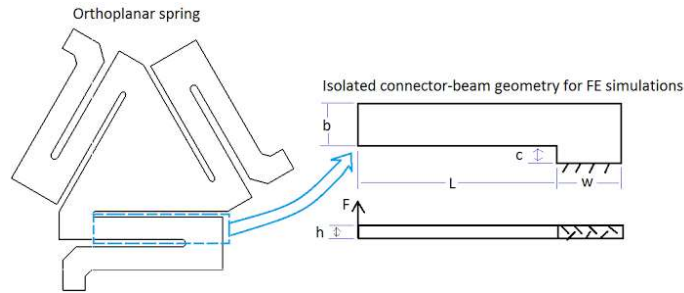


**Figure A.1:** Geometry for determining effective beam length relationship using finite elements.

**Table A.1:** Data used to determine  $f(b/c, b/h)$ .

$\delta L_{eff}/c$	$b/c$	$b/h$	$\delta L_{eff}/c$	$b/c$	$b/h$	$\delta L_{eff}/c$	$b/c$	$b/h$
2.5765	5	3.1496	2.6209	5	3.1496	2.4286	5	10
1.7510	2.5	1.5748	2.5574	5	3.1496	1.9162	3.75	7.5
3.4332	7.5	4.7244	2.5638	5	3.1496	1.7596	3	2.8346
2.9960	6.25	3.9371	2.3634	5	5	3.2766	8	8
2.1635	3.75	2.3622	2.8692	5	2	4.6403	12	12
8.1088	20	3.1496	2.5987	5	3.1496	3.1204	7	6.5
4.4981	10	3.1496	2.5411	5	3.1496	3.7190	8	3
1.9023	3.3333	3.1496	2.4034	4.5	2.8346			
2.8721	5	3.1496	1.3496	2.25	4.5			

## Appendix B: Stress Concentration Factor

Section 4.2 analyzed the stresses that develop in the orthoplanar spring and presented equations for estimating the stress concentration factor. Finite element analysis was performed on a cantilevered beam geometry with a stress concentration similar to that present at the ends of the beam segments of the orthoplanar spring. The maximum bending stress determined by finite element analysis was compared to the nominal bending stress calculated by the standard flexure formula to determine stress concentration factors. Bending stress concentration factor data is plotted against the fillet radius-to-beam width ratio for varying beam width-to-thickness ratios in Figure B.1.

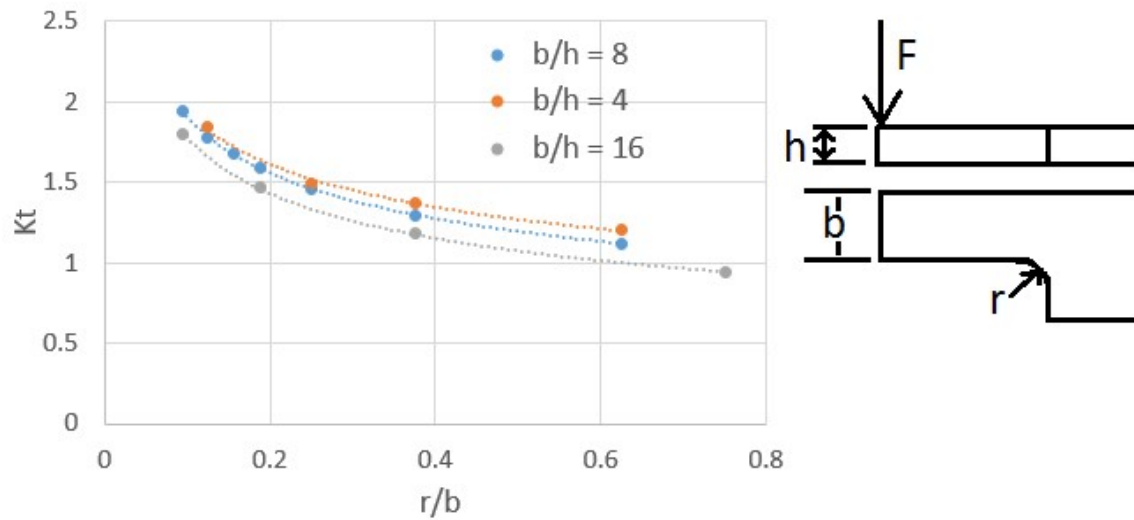


Figure B.1: Stress concentration factor.

## Appendix C: Orthoplanar Spring Designs Used in Finite Element Analysis Validations

Four orthoplanar spring designs were used to validate the compliance and stress analysis presented in sections 4.1 and 4.2. The designs used in the finite element analysis are specified in Table C.1, and the design parameters are defined in Figure C.1. Each design used the same material with an elastic modulus of 2900 MPa and a Poisson ratio of 0.35 and each design had a fillet radius of 2 mm. The results were presented in section 4.3.

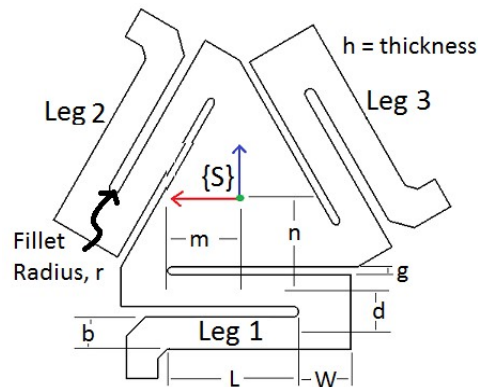


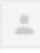


Figure C.1 Design parameters of orthoplanar spring.


Table C.1: Design parameters of orthoplanar springs used in finite element analysis.

Parameters	Design 1	Design 2	Design 3	Design 4
$b$	12	9	9	12
$h$	3.175	3.175	3.75	5
$L$	50	50	60	50
$m$	-27.5	-27.5	-24	-27.5
$n$	35	35	30	35
$d$	16	13	15	16
$w$	20	20	20	20
$g$	3	3	3	3

## Appendix D: Copyright Permissions

Permissions for using Figure 3.1 was granted in the following email.

 **Jerry West** <jerrywest@mail.usf.edu> Feb 13 (1 day ago) ☆  




to Redwan 


Hello Dr. Alqasemi,

I would like to request copyright clearance for using figure 3.1 from your dissertation- "Maximizing manipulation capabilities of persons with disabilities using a smart 9-degree-of-freedom wheelchair-mounted robotic arm system" in my thesis- "Orthoplanar Spring Based Compliant Force/Torque Sensor for Robot Force Control". Thank you.

Best Regards,  
Jerry

---

 **Alqasemi, Redwan** 2:06 PM (23 hours ago) ★  

to me 

Permission granted.

---

Redwan Alqasemi, Ph.D.  
Research Professor, Department of Mechanical Engineering  
Center for Assistive, Rehabilitation & Robotics Technologies (CARRT)  
University of South Florida  
4202 E. Fowler Avenue, ENB 118  
Tampa, FL 33620  
[+1\(813\)974-2115](tel:+18139742115)